Anomalous diffusion of synaptic vesicles and its influences on spontaneous and evoked neurotransmission

Jacopo Lamanna[1,2] , Giulia Gloria[1] , Antonello Villa[3] and Antonio Malgaroli[1,2,4]

[1]*Center for Behavioral Neuroscience and Communication (BNC), Vita-Salute San Raffaele University, Milan, Italy*
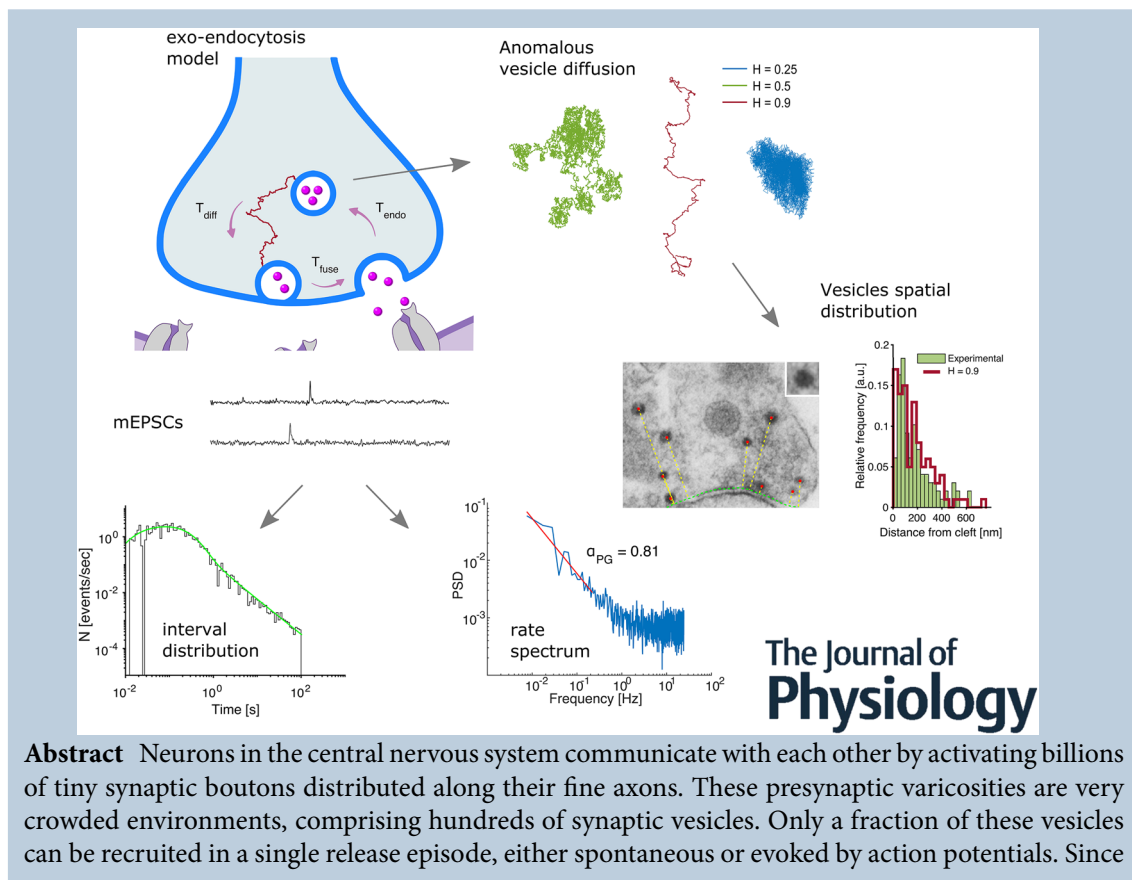[2]*Faculty of Psychology, Vita-Salute San Raffaele University, Milan, Italy*
[3]*Consorzio MIA, University of Milano-Bicocca, Milan, Italy*
[4]*San Raffaele Turro, IRCCS Ospedale San Raffaele, Milan, Italy*

Handling Editors: David Wyllie & Srikanth Ramaswamy

The peer review history is available in the Supporting Information section of this article (https://doi.org/10.1113/JP284926#support-information-section).

Abstract Neurons in the central nervous system communicate with each other by activating billions of tiny synaptic boutons distributed along their fine axons. These presynaptic varicosities are very crowded environments, comprising hundreds of synaptic vesicles. Only a fraction of these vesicles can be recruited in a single release episode, either spontaneous or evoked by action potentials. Since

Jacopo Lamanna obtained his PhD in Bioengineering at Polytechnic University of Milan (Italy) in 2013, after which he worked as a post-doc research fellow at the Neurobiology of Learning Unit of San Raffaele Scientific Institute (Milan) where he applied *in vitro* and *in vivo* electrophysiology to study synaptic transmission and plasticity. Since 2016 he has been Assistant Professor of Physiology at Faculty of Psychology, Vita-Salute San Raffaele University (Milan). In 2017 he received the NARSAD Young Investigator Grant (BBRF, New York, USA). His main research interests include the physiological bases of synaptic transmission and plasticity and their role in animal behaviour and mental disorders.

the seminal work by Fatt and Katz, spontaneous release has been modelled as a memoryless process. Nevertheless, at central synapses, experimental evidence indicates more complex features, including non-exponential distributions of release intervals and power-law behaviour in their rate. To describe these features, we developed a probabilistic model of spontaneous release based on Brownian motion of synaptic vesicles in the presynaptic environment. To account for different diffusion regimes, we based our simulations on fractional Brownian motion. We show that this model can predict both deviation from the Poisson hypothesis and power-law features in experimental quantal release series, thus suggesting that the vesicular motion by diffusion could *per se* explain the emergence of these properties. We demonstrate the efficacy of our modelling approach using electrophysiological recordings at single synaptic boutons and ultrastructural data. When this approach was used to simulate evoked responses, we found that the replenishment of the readily releasable pool driven by Brownian motion of vesicles can reproduce the characteristic binomial release distributions seen experimentally. We believe that our modelling approach supports the idea that vesicle diffusion and readily releasable pool dynamics are crucial factors for the physiological functioning of neuronal communication.

Corresponding authors J. Lamanna and A. Malgaroli: Centre for Behavioral Neuroscience and Communication (BNC), Faculty of Psychology, Vita-Salute San Raffaele University, Via Olgettina 58, Milan 20132, Italy. Email: lamanna.jacopo@hsr.it and malgaroli.antonio@unisr.it

Abstract figure legend A novel model of synaptic vesicle exo-endocytosis was developed, based on vesicles' anomalous diffusion before their docking to the presynaptic active zone. Different regimes of diffusion, from sub-diffusion to super-diffusion, including Brownian motion, can be modelled by fractal Brownian motion with different values of the Hurst exponent, H. Predicted spatial distributions of recycling vesicles fit ultrastructural data. Importantly, the model correctly predicts complex features of spontaneous neurotransmission, including heavy-tailed distributions of miniature excitatory post-synaptic currents recorded at single synaptic boutons as well as power-law spectra of their rate. The model provides insights into the dynamics of the readily releasable pool of synaptic vesicles and their effect on action potential evoked neurotransmission.

Key points

- We developed a new probabilistic model of spontaneous and evoked vesicle fusion based on simple biophysical assumptions, including the motion of vesicles before they dock to the release site.
- We provide closed-form equations for the interval distribution of spontaneous releases in the special case of Brownian diffusion of vesicles, showing that a power-law heavy tail is generated.
- Fractional Brownian motion (fBm) was exploited to simulate anomalous vesicle diffusion, including directed and non-directed motion, by varying the Hurst exponent.
- We show that our model predicts non-linear features observed in experimental spontaneous quantal release series as well as ultrastructural data of synaptic vesicles spatial distribution.
- Evoked exocytosis based on a diffusion-replenished readily releasable pool might explain the emergence of power-law behaviour in neuronal activity.

Introduction

Understanding the fine mechanisms behind neuronal communication is a primary goal in neuroscience, since it is very likely that the extraordinary computational power of our brains resides in these still nebulous processes. Neurons in the central nervous system communicate with each other by activating billions of tiny synaptic boutons distributed along their fine axons. These presynaptic varicosities are very crowded environments, comprising thousands of distinct protein species and hundreds of synaptic vesicles. Only some of these vesicles are actively recycled to sustain the quantal discharge of neurotransmitter molecules, which occurs both spontaneously and upon the arrival of action potentials, while the others await future recruitment in a reserved pool. Spontaneous and evoked release have been extensively investigated for their interactions, and two opposite perspectives

have emerged: on the one hand, the two processes were initially thought to share the same biochemical mechanisms, molecular machinery and vesicles (Wilhelm et al., 2010); in recent years, several authors provided extensive evidence supporting separate pathways and vesicles for the two processes (Chung et al., 2010; Kavalali, 2015; Peng et al., 2012; Sara et al., 2005).

Since the seminal work by Fatt & Katz (1952), spontaneous vesicle fusion has been modelled as a memoryless process, well described by a Poisson point process with exponential distribution of intervals among successive release events. In the last decades, evidence has accumulated denying this prediction for central synapses: both non-homogeneity of the release rate (Abenavoli et al., 2000; Forti et al., 1997) and non-linear features (Lamanna et al., 2011, 2015; Lowen et al., 1997) are clearly present, but these have never been considered together in a complete model. On the other hand, evoked release driven by action potentials is universally modelled using a binomial model, where a fixed pool of readily releasable vesicles (RRP), docked to the presynaptic membrane, have a common probability of being randomly discharged when the action potential triggers a calcium rise in their proximity. Powerful quantal analysis methods (Bykowska et al., 2019), including Bayesian approaches, have been developed in the last decades for obtaining unbiased and efficient estimators for number of sites (N), release probability (p), and quantal amplitude from recorded postsynaptic responses. Unfortunately, the underlying assumptions about the RRP and the fusion process still do not enable the capture of the sources of non-linearity that have been shown to emerge in neuronal activity at several levels of the CNS. Beside not being able to reproduce the aforementioned experimental features, both the Poisson and binomial models do not account for the previous history of vesicles, e.g. their motion in the presynaptic compartment before docking to the membrane.

Our understanding of vesicle motion in the synaptic boutons remained limited until sufficient resolution was achieved by advanced microscopy techniques. Seminal studies applied total internal reflection fluorescence (TIRF) microscopy to very large terminals, the ribbon of retina bipolar cells, gathering important clues about vesicle mobility and localization before and during the fusion process: vesicles involved in recycling are mobile, as opposed to resting ones, and reach the cytoplasmic membrane with similar timing independent of their final spot, but they fuse with much higher probability and speed at active zones (Zenlsek et al., 2000). With the introduction of super-resolution microscopy, similar observations were obtained at hippocampal neurons synapses, and further details emerged (Westphal et al., 2008). According to these studies, stimulation of action potentials does not affect vesicle motion, but only fusion probability (Kamin et al., 2010), although recent evidence contradicts this conclusion. In addition, patches of membrane resulting from fully collapsed vesicles remain stable in their molecular composition to be later retrieved by the clathrin machinery and become mobile again for recycling (Kamin et al., 2010). More recent studies succeeded in tracking the 3D motion of synaptic vesicles with high resolution and confirmed that in control conditions vesicles from the RRP remain close to their fusion site after retrieval (Chen et al., 2021).

Importantly, all the above studies suggest that vesicles motion represents a substantial fraction of vesicles' lifetime before fusion, and thus these dynamics are likely to be reflected in their recycling. This aspect is of particular importance at central presynaptic terminals, where a few vesicles (<20) have been estimated to reside in the docked pool (Schikorski & Stevens, 2001). As a matter of fact, we can argue that the replenishment of this pool is mostly driven by vesicle diffusive motion, whose temporal dynamics would affect the 'instantaneous' number of RRP vesicles: each vesicle, after its flight in the presynaptic milieu, will eventually dock to the presynaptic membrane and go through spontaneous or evoked fusion after a variable period. A natural consequence of this scenario is that the timing of spontaneous quantal discharges and the quantal amplitude of evoked transmission will both, at least in part, reflect the motion dynamics. Interestingly, vesicle motion appears as a very complex phenomenon, due to the crowded presynaptic environment that causes stick-and-diffuse, but also to the molecular motors involved (Chung et al., 2010; Kneussel & Wagner, 2013; Maschi et al., 2018). In this context, single vesicle tracking has evidenced both free and directed regimes of motion that can stochastically switch during vesicle flight (Joensuu et al., 2016) and whose relative proportion can significantly differ between vesicles involved in spontaneous and evoked fusions, the latter more often involving molecular motors (Peng et al., 2012). These forms of motion are generally regarded as non-Brownian anomalous diffusion, and one of the most comprehensive approaches for the modelling of such motions is fractional Brownian motion (fBm) with varying Hurst exponent, H (Han et al., 2020), where $H = 0.5$ for pure Brownian motion typical of free diffusion, $H < 0.5$ for sub-diffusive motion in really crowded environments, and $H > 0.5$ for super-diffusive (directed) motion where molecular motors are involved.

In this work, we developed a probabilistic model based on simple biophysical assumptions, which includes the motion of vesicles before they dock to the release site. Starting from our simulations and analyses, we then show that this model can reproduce both deviation from the Poisson hypothesis and power-law features for spontaneous quantal release series. In addition, this model provides useful insights into the negative consequences of abnormal synaptic vesicle motion, which has been

recently implicated in models of mental disorders (Chen et al., 2021).

Methods

Ethical approval

Research and animal care procedures were approved by our Institutional Animal Care and Use Committee for Good Animal Experimentation, in accordance with the Italian Ministero della Salute code of practice for the care and use of animals for scientific purposes (IACUC number: 728). Sprague–Dawley newborn rats (P2–P5; both sexes; CD strain), together with SD dams were acquired from Charles River (Milan, Italy). SD dams were always supplied with *ad libitum* food and water. All effort was made to minimize the rats' distress, and humane killing procedure were used: sevoflurane overdose for dams; neck dislocation for newborns of P2–P5.

Simulation of fractional Brownian motion

All data simulations and analysis as well as data representations were performed using custom algorithms developed in MATLAB (The MathWorks, Natick, MA, USA).

To simulate 1D fBm we employed an algorithm based on a fast Fourier transform (FFT) providing a good trade-off between simulation accuracy and speed of computation (Botev, 2016; Kroese & Botev, 2013). This algorithm allows us to generate a series of motion steps which are distributed as a gaussian, and whose temporal structure shows long-term correlation for specific ranges of H (while for $H = 0.5$ it produces the standard Brownian motion). For completeness, we provide details of the algorithm here.

In brief, the algorithm simulates the fBm $\{W_t, t \geq 0\}$ with covariance function:

$$\mathrm{cov}\,(W_t, W_s) = \frac{1}{2}\,\left(|t|^{2H} + |t|^{2H} - |t - s|^{2H}\right), t, s \geq 0 \quad (1)$$

where $H \in (0, 1)$ is the Hurst exponent, by first generating a fractional Gaussian noise (fGn) X_i with covariance function:

$$\mathrm{cov}\,(X_i, X_{i+k}) = \frac{1}{2}\,\left(|k + 1|^{2H} - 2|k|^{2H} + |k - 1|^{2H}\right),$$
$$k = 0, 1, 2, \ldots \quad (2)$$

Simulation of fBm on the uniformly spaced grid $0 = t_0 < t_1 < t_2 < \ldots < t_n = 1$ can be obtained by generating the increment process $\{X_1, X_2, \ldots, X_n\}$, where $\{X_i = W_i$

$- W_{i-1}\}$ (Botev, 2016; Kroese & Botev, 2013), and finally delivering the cumulative sum:

$$W_{t_i} = c^H \sum_{k=1}^{i} X_k,\ i = 1, \ldots, n, c = \frac{1}{n} \quad (3)$$

We set $n = 100{,}000$, since this number of samples was sufficient to get a second zero-crossing by the fBm (including the starting point $W_0 = 0$) in almost all cases. If the simulation failed to reach a zero-crossing, it was discarded and a new fBm simulation was generated.

Simulation of the release time series

The series of time intervals between successive release events from one vesicle was generated using the full model: $T_{\mathrm{rel}} \approx T_{\mathrm{diff}} + T_{\mathrm{fuse}}$. To account for different conditions of vesicle diffusion (sub-diffusive and super-diffusive regimes), we simulated, as described above, a fractional Brownian motion (fBm) trajectory with a dT of 35 ms, as the fBm sampling time and the following values of the Hurst exponent H: 0.1, 0.25, 0.5, 0.75, 0.9. T_{diff} is the first return time of a 1D fBm to the origin (i.e. the first zero crossing for $t > 0$). To simulate T_{fuse}, we generated time intervals following the exponential distribution $\exp(\mu)$ we opted for generating simulations with different μ values (0.1, 1, 10, 100 s). The time required by the vesicle to spontaneously fuse after the new docking event was extracted from an exponential distribution with mean parameter μ using the exprnd () function of the statistical toolbox of MATLAB. T_{endo} was generated using another mono-exponential distribution with mean parameter equal to 12 s. In indicated cases, we linearly scaled the series of fusions to obtain a standard average fusion frequency for sake of comparability ($N_{\max}/T_{\max} = 0.1$ Hz).

Log-binned histograms for interval distributions

Due to the heavy-tail nature of the involved distributions and to previous reports (Abenavoli et al., 2000, 2002; Lamanna et al., 2012), we decided to generate histograms of simulated intervals according to a logarithmically binned representation (McManus et al., 1987; Sigworth & Sine, 1987). Furthermore, such a representation provides a direct comparison of our simulated data with both real and simulated data of single-synapse recordings described before (Abenavoli et al., 2000, 2002; Lamanna et al., 2012). For such a representation, intervals between successive simulated events were binned according to the logarithm of their duration. This produces an increase in bin width as interval duration increases. The number of intervals falling in each bin (bin content) was divided by bin width to obtain a normalized bin content, which was then shown

as a function of bin centre on a doubly logarithmic scale. The produced graphs provide easy evaluation of produced interval distributions on the whole range of intervals including long tails containing few events.

Power-law fitting of interval distributions

To fit our interval distributions to power laws and estimating the exponent, we adopted discrete and continuous maximum-likelihood fitting together with a goodness-of-fit based approach to set the lower cut-off for the scaling region, according to the method described by Clauset et al. (2007). Let x be a vector of observations of some quantity to which the power-law distribution $P(x) \sim x^{-\alpha}$ must be fitted for $x \geq x_{min}$. The algorithm automatically detects whether x consists of real or integer values and adopts the most appropriate method. In the first place, for each possible x_{min}, α is estimated through the maximum-likelihood method, and the Kolmogorov–Smirnov goodness-of-fit statistic D is computed. Then, the value of x_{min} giving the minimum D was selected as the lower bound of the power-law behaviour and the obtained α corresponds to the maximum-likelihood estimate of the scaling exponent, with L being the log-likelihood of the data under the fitted power-law.

Quantification of fractal behaviour: periodogram and Allan factor

We selected two separate methods for the quantification of fractal behaviour, the periodogram (PG) and the Allan factor (AF). Besides being the most reliable and accurate methods reported in literature for the quantitative estimation of fractal exponents (Lowen & Teich, 2005), these were already adopted for analysis of non-linear features in a temporal series of quantal release (Lamanna et al., 2011, 2012, 2015; Lowen et al., 1997). Periodogram-based quantification was implemented according to previously published algorithms (Lowen & Teich, 2005; Thurner et al., 1997). The length of the series is divided in contiguous windows of length T. $C = L/T$ series Y_i are then obtained, by further dividing each window in M segments of 0.1 s (fixed resolution) and counting the number of events falling in each segment. A periodogram (PG) is then computed for each windowed series as $S_w(f) = \frac{1}{M} \bar{Y}(f)^2$ where $\bar{Y}(f)$ is the discrete Fourier transform of the series Y_i. The obtained PGs are then averaged to obtain the final count-based PG $S(f)$. For fractal-rate point processes, the count-based PG follows a power-law of the form $f^{-\alpha_{PG}}$ in the low-medium frequency range, where α is the fractal exponent. We estimated α_{PG} by linear least-mean-square regression on a doubly logarithmic scale, log10(PG) *vs.*

log10(f), excluding $F = 0$ and imposing a fixed cut-off frequency. The Allan factor is a normalized version of Allan variance, it was computed as:

$$\mathrm{AF}(\tau) = E\left[\frac{(Z_{k+1} - Z_k)^2}{2E[Z_k]}\right], \tag{4}$$

where Z_k is the count series obtained using a count window of length τ (Lowen & Teich, 2005). The AF for a fractal point process assumes the power-law form $\mathrm{AF}(\tau) \approx 1 + (\frac{\tau}{\tau_0})^{\alpha_{AF}}$ with fractal onset time τ_0. Estimating of α_{AF} was achieved by linear least-mean-square regression on doubly logarithmic scale, log10(AF) *vs.* log10(τ), from $\tau_0 = 1$.

CA3–CA1 hippocampal cultures

Primary postnatal CA3–CA1 neuronal cultures were prepared from Sprague–Dawley rats (2–5 days old) as previously described (Lamanna et al., 2015; Malgaroli et al., 1995). Briefly, P2–P5 rats of both sexes were killed by neck dislocation followed by decapitation and the CA3–CA1 region of hippocampus dissected out. Dissociated neurons were grown on poly-L-ornithine (10 μg ml^{-1}) and Matrigel (1:50 dilution; BD Biosciences, San Jose, CA, USA) coated 24 mm glass coverslips in 35 mm petri dishes (BD Falcon). Neurons were maintained in a CO_2 incubator (5% CO_2, 37°C; Heraeus Instruments GmbH, Hanau, Germany) using a modified minimum essential medium (MEM) with Earle's salts (Thermo Fisher Scientific, Waltham, MA, USA) in 5% dialysed fetal bovine serum (Thermo Fisher Scientific). The MEM was supplemented with insulin (30 mg l^{-1}), biotin (0.1 mg l^{-1}), vitamin B12 (1.5 mg l^{-1}), L-ascorbic acid (100 mg l^{-1}), transferrin (100 mg l^{-1}; Merck KGaA, Darmstadt, Germany), Glutamax (100 mg l^{-1}; Thermo Fisher Scientific), D-glucose (6 g l^{-1}), HEPES (3.6 g l^{-1}), gentamicin (2 mg l^{-1}). Every 3 days one-third of the culture medium was replaced with fresh medium supplemented with cytosine β-D-arabinofuranoside (ARA-C; 2.5–5 μM) to prevent excessive glial cells proliferation. If not otherwise indicated, salts and chemicals were obtained from Sigma-Aldrich (St Louis, MO, USA).

Electrophysiological recordings

CA3–CA1 cultured neurons were used for electro-physiological experiments 10–21 days after plating. All electrophysiological recordings were performed at room temperature (24°C) and neurons were continuously super-fused (1–2 ml/min) with a Tyrode solution containing (in mM): 119 NaCl, 5 KCl, 2 $CaCl_2$, 2 $MgCl_2$, 25 HEPES, and 30 D-glucose. This solution was supplemented with the GABA$_A$ receptor blocker picrotoxin (PTX; 100 μM),

tetrodotoxin (TTX), and the NMDA receptor blocker D-2-amino-phosphonovalerate (APV; 25 μM; Tocris Cookson, Bristol, UK). Solution osmolarity was adjusted to 305 mOsm and pH to 7.4.

Synaptic bouton visualization was obtained either by transduction of cultures with a lentivirus carrying an eGFP-VAMP2 construct, eGFP-SynaptoZip (Ferro et al., 2017; Lamanna, Isotti, et al., 2022) or by staining for 1–2 min with 10 μM FM1-43 dissolved in modified Tyrode solutions (5 mM CaCl$_2$/no added MgCl$_2$; 25 μM 6-cyano-7-nitro-quinoxaline-2,3-dione (CNQX; Tocris), 0.5–1 mM kynurenate (Tocris)). Loose-patch synaptic recordings were performed as previously described (Forti et al., 1997). In brief, patch pipette electrodes for loose patch (resistance 1–2 MΩ) were filled with a modified extracellular solution (CaCl$_2$ 5 mM (no added MgCl$_2$), picrotoxin 100 μM, APV 25 μM, TTX 0.5 μM). Pipettes were lowered to enclose selected boutons without suction. Currents were acquired in voltage clamp (holding potential 0 mV; Axopatch 200B amplifier; Axon Instruments, Foster City, CA, USA). Seal resistance (<10 MΩ) was monitored by applying 2 mV depolarizing pulses. Current traces were filtered at 2–5 kHz and digitally acquired at 20 kHz using a 16-bit analog-to-digital interface (HEKA ITC-18; HEKA Elektronik, Lambrecht/Pfalz, Germany) controlled by a C/C++ acquisition software developed in house. Minis were detected semi-automatically using a custom graphical user interface developed in MATLAB.

Synaptic vesicle labelling by horseradish peroxidase and electron microscopy

Hippocampal cultures were washed with standard Tyrode solution (37°C) and bathed in the same solution supplemented with horseradish peroxidase (HRP; 10 mg/ml). Cells were then stimulated at 0.5 Hz for 10 min using platinum field electrodes (1 ms pulses; 20 mV/cm). The morphology of the electrodes, the distance between anode and cathode and the field intensity were established, prior to the experiments, by electrophysiological recordings and FM1-43 (Thermo Fisher Scientific) synaptic uptake experiments. At the end of stimulation epochs, to remove extracellular HRP, neurons were quickly washed a few times with a Tyrode solution (4°C) supplemented with TTX (1 μM; Latoxan, Valence, France). For pre-embedding staining of vesicles containing HRP, neurons were lightly fixed (2% glutaraldehyde; 10 min) and incubated for 30 min in a solution containing 0.05% (w/v) diaminobenzidine (DAB) and 0.01% (v/v) hydrogen peroxide. After a few wash cycles, neurons were re-exposed to a fixative solution (2% glutaraldehyde, 4% formaldehyde in 0.1 M cacodylate buffer) for 45 min. For standard electron

microscopy analysis the detailed procedure has been previously described (Böse et al., 2000). In brief, cells were post-fixed with 2% OsO4. After dehydration in ethanol and overnight infiltration (75% Epon 812 and 25% ethanol), samples were embedded in Epon and ultrathin serial sections ($\sim$60 nm) obtained. These were doubly stained with uranyl acetate and lead citrate and examined with a Hitachi H-7000 microscope. In these experiments $n = 36$ synapses with evoked HRP uptake were reconstructed, and $n = 3$ could be fully reconstructed through sections and used for the analyses based on custom algorithms developed in MATLAB for measuring vesicles distances from presynaptic membranes. Vesicles were manually selected to exclude large dense core vesicles and HRP labelled endosomal structures, the latter were carefully searched and identified across the serial sections.

Results

Spontaneous synaptic vesicle motion and recycling: model development

To develop our model, we simulated a stick and diffuse process where vesicles: (1) dock to the presynaptic membrane; (2) fuse spontaneously after a period T_{fuse}; (3) are endocytosed to be recycled in a time T_{endo}; (4) diffuse in the presynaptic compartment for a period T_{diff}, until they come back to the docking site (Fig. 1A).

Hence, the series of time intervals between successive release events from a single vesicle is generated using the following equation: $T_{\text{rel}} = T_{\text{diff}} + T_{\text{fuse}} + T_{\text{endo}}$. To account for different conditions of vesicle diffusion in generating T_{diff} values, from sub-diffusive to super-diffusive regimes, including free and directed motion, we opted for simulating a fractional Brownian motion (fBm) trajectory with different values of the Hurst exponent H (see Methods for details). We assumed that the recently retrieved vesicle moves in the presynaptic cytoplasm (3D) starting from the presynaptic membrane surface (2D) and then must return, after a time T_{diff}, to that surface for docking. Hence, in our model, T_{diff} equals to the first return time of the 3D fBm to the membrane surface, which can be simplified as the first return time of a 1D fBm to the origin (i.e. the first zero crossing for $t > 0$), if we assume the membrane surface to be flat and orthogonal to the direction of the 1D fBm, which is reasonable at least in an area close to the fusion site. Figure 1B shows the log-binned histograms (a convenient approach for heavy-tailed distributions; see methods for details) of T_{diff} values obtained simulating fBm with different H values (0.25, 0.5 and 0.9), together with exemplar 2D fBm trajectories. The estimated distributions display a heavy-tailed power-law profile reminiscent of the Lévy distribution, a stable distribution. This is not surprising,

since the closed-form probability density function (pdf) for the first return time of the pure Brownian motion (fBm with $H = 0.5$) for large t approaches the Lévy stable distribution with location parameter $l = \frac{1}{2}$ and scale parameter $C = 2\sqrt{D}$ where $D > 0$ is the diffusion constant (Sornette, 2006). To simulate T_{fuse}, we generated time intervals following the exponential distribution with mean μ, to account for the memoryless and spontaneous nature of the fusion process. It is worth noting that T_{fuse} represents only the final step of our release model, which is the time interval from vesicle docking to its fusion. Since accurate experimental estimations of μ are not available, we opted for generating simulations with different μ values (0.1–100 s), indicating experimental conditions over a broad range of release probability (exemplar log-binned representation of exponential distributions for the simulated values of μ are shown in

Fig. 1C). Finally, T_{endo} was generated using an exponential distribution with mean parameter equal to 12 s, a value in line with was has been obtained experimentally at central synapses (Chanaday & Kavalali, 2018; Granseth et al., 2006).

For the special case of Brownian motion ($H = 0.5$), we obtained a closed-form expression for the pdf of T_{rel} by convolution. More specifically, $T_{fuse} + T_{endo}$ follows the hypoexponential distribution with parameters λ_1, λ_2, Hypo(λ_1, λ_2), whose pdf is:

$$f_1(x) = \frac{\left(-e^{-\lambda_1 t} + e^{-\lambda_2 t}\right)\lambda_1\lambda_2}{\lambda_1 - \lambda_2},$$
$$x \geq 0 \wedge \lambda_1 \geq 0 \wedge \lambda_2 \geq 0, \tag{5}$$

while T_{diff} for BM ($H = 0.5$) was modelled with the Lévy (0.5, C) distribution (Sornette, 2006) whose pdf is:
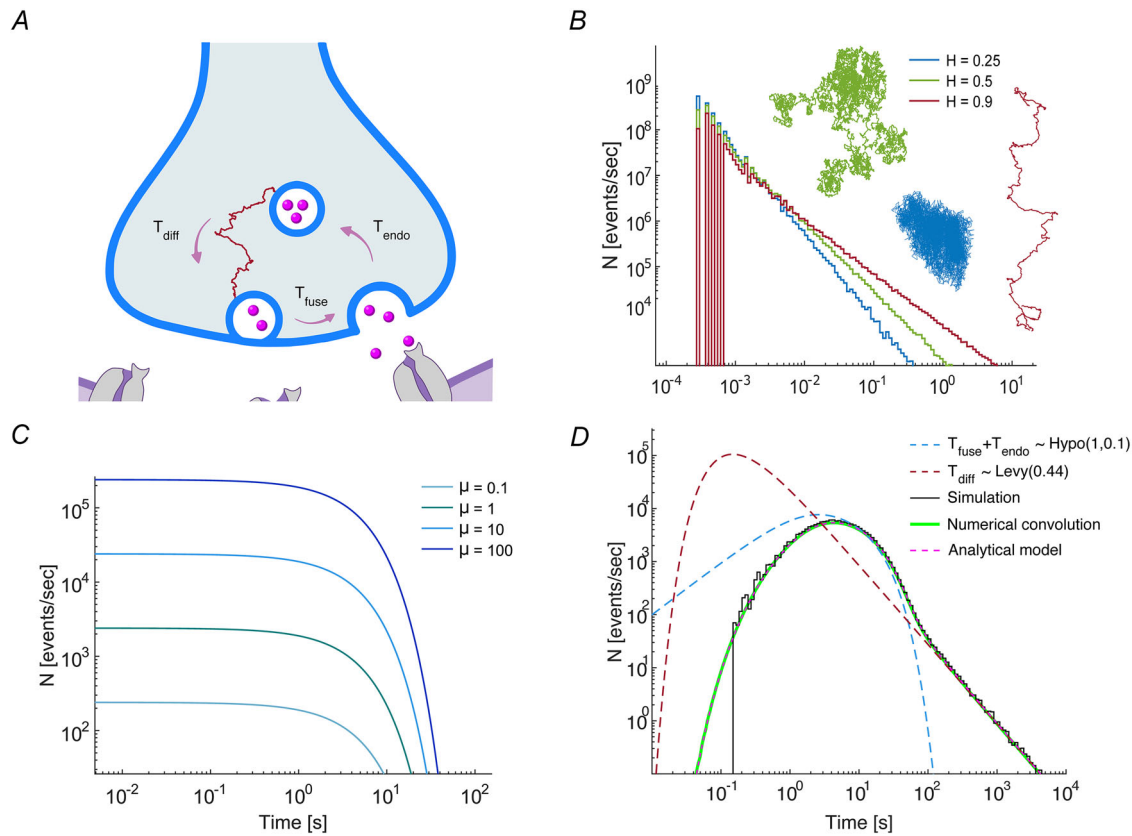
Figure 1. Development of a dynamic model of spontaneous synaptic vesicle recycling
A, cartoon illustrating the model transitions, where T_{diff} represents the return time of the vesicle to the release site by diffusion, T_{fuse} equals the time required to spontaneously fuse after docking at the presynaptic membrane, and T_{endo} accounts for the time of endocytosis. *B*, log-binned histograms of simulated T_{diff} for different diffusive regimes, obtained from 1D fBm with $H = 0.25$ (blue, sub-diffusion), $H = 0.5$ (green, Brownian motion), $H = 0.9$ (red, super-diffusion). *C*, logarithmic plot of the exponential distributions describing T_{fuse}, for different values of μ (0.1–100 s). *D*, log-binned histogram (black line) of simulated T_{rel} for $H = 0.5$ (Brownian motion), with overlaid probability density function (pdf) of: (1) $T_{fuse} + T_{endo} \sim$ Hypo(1, 0.1) (blue dashed line, see eqn 5); (2) $T_{diff} \sim$ Lévy (0.5, $\sqrt{0.44}$) (dashed red line, see eqn 6); (3) analytical model of T_{rel} with, $C = \sqrt{0.44}$, $\lambda_1 = 1$ and $\lambda_2 = 0.1$ (see eqn 8). The graph also shows the numerical solution for convolution of the two parental pdfs (green line, see eqn 7), which coincides with the analytical model's pdf. [Colour figure can be viewed at wileyonlinelibrary.com]

$$f_2(x) = \frac{Ce^{\frac{-C^2}{2x}}}{\sqrt{2\pi}\,x^{3/2}}, \; x \geq 0 \wedge C = 2\sqrt{D} \wedge D > 0. \quad (6)$$

Hence, the pdf of T_{rel} was obtained by solving the convolution integral between $f_1(x)$ and $f_2(x)$:

$$f_{rel}(x) = \int_0^x f_1(t) f_2(x - t)$$

$$dt = \int_0^x \frac{Ce^{\frac{C^2}{2(t-x)}}\left(-e^{-\lambda_1 t} + e^{-\lambda_2 t}\right)\lambda_1\lambda_2}{(\lambda_1 - \lambda_2)\sqrt{2\pi}(x-t)^{\frac{3}{2}}}$$

$$dt = \frac{\lambda_1\lambda_2}{2(\lambda_1 - \lambda_2)}\left(-e^{-iC\sqrt{2\lambda_1} - \lambda_1 x}\left(\text{erfc}\left(\frac{C}{\sqrt{2x}} - i\sqrt{\lambda_1}x\right)\right.\right.$$

$$+ e^{2iC\sqrt{2\lambda_1}}\text{erfc}\left(\frac{C}{\sqrt{2x}} + i\sqrt{\lambda_1}x\right)\bigg)$$

$$+ e^{-iC\sqrt{2\lambda_2} - \lambda_2 x}\left(\text{erfc}\left(\frac{C}{\sqrt{2x}} - i\sqrt{\lambda_2}x\right)\right.$$

$$+ e^{2iC\sqrt{2\lambda_2}}\text{erfc}\left(\frac{C}{\sqrt{2x}} + i\sqrt{\lambda_2}x\right)\bigg)\bigg). \quad (7)$$

The closed-form expression of eqn (7) can be further simplified as:

$$f_{rel}(x) = \frac{\lambda_1\lambda_2}{\lambda_1 - \lambda_2}\left(-e^{-\lambda_1 x}Re\left(e^{i\sqrt{2}C\sqrt{\lambda_1}}\text{erfc}\right.\right.$$

$$\left(\frac{C}{\sqrt{2x}} + i\sqrt{\lambda_1}x\right)\bigg)$$

$$+ e^{-\lambda_2 x}Re\left(e^{i\sqrt{2}C\sqrt{\lambda_2}}\text{erfc}\left(\frac{C}{\sqrt{2x}} + i\sqrt{\lambda_2}x\right)\right)\bigg),(8)$$

(see appendix for details). From the latter expression it results that the pdf will assume only real values, as expected for a biophysical system.

Although this analytical solution represents only a partial prevision (limited to $H = 0.5$) of the spontaneous fusion regimes generated by our mol, it gives an idea of the potential influence of vesicle motion on the overall release dynamics, which is a power-law decay for large intervals, whose exponent is $-3/2$ for the ordinary BM (Rangarajan & Ding, 2000; Sornette, 2006). Figure 1*D* shows an overlay of the three pdfs of eqns (5), (6), and (8) on logarithmic axes for $\lambda_1 = 1 \text{ s}^{-1}$, $\lambda_2 = 0.1 \text{ s}^{-1}$, and $C = \sqrt{0.44}$ (corresponding to $D = 0.11 \, \mu\text{m s}^{-1}$). In the same panel, the log-binned histogram of a simulation based on the sum of random samples from the three distributions is shown (black line) together with the numerical solution of the convolution integral (green line) (Fig. 1*D*). As can be appreciated from the graph, the analytical model optimally fits the simulated data and coincides with the numerical convolution.

Table 1. Mean ± SD of the observed α values obtained fitting the histogram of T_{diff} values obtained with 100 fBm simulations with the selected Hurst parameters (theoretical prediction in the third column)

| Hurst parameter	Mean observed α	Expected α
0.1	−1.91 (± 0.097)	−1.90
0.25	−1.76 (± 0.073)	−1.75
0.5	−1.55 (± 0.039)	−1.50
0.75	−1.37 (± 0.019)	−1.25
0.9	−1.29 (± 0.125)	−1.10

$n = 100,000$ fBm samples for each series.

Simulations of spontaneous fusions for synaptic vesicles with different diffusive regimes and release probabilities

We then performed the first set of simulations of release series (T_{rel}) for a single vesicle varying the H parameter of the fBm in the range 0.1–0.9. Figure 2 shows the log-binned histograms of simulations with different fusion probabilities: high probability, $\mu = 0.1$ s (Fig. 2*A*) and low probability, $\mu = 100$ s (Fig. 2*B*). It is clear from these graphs that in the former case the fBm produces power-law behaviour in these release series for larger intervals (straight line in doubly logarithmic plot), while for shorter intervals the classical exponential distribution is predominant. On the contrary, when fusion probability is low, such behaviour is lost even at very large intervals (Fig. 2*B*).

We then analysed the relationship between the H exponent of the fBm and the slope of the power-law behaviour observed in interval distributions, $P(t) \sim t^\alpha$, as the latter is introduced by the fBm dynamics, as discussed above. To obtain a good estimate, we performed a maximum likelihood fitting of the scaling exponent α on the log-binned histograms by applying a goodness-of-fit based approach (Clauset et al., 2007). Figure 2*C* shows three exemplar histograms for high fusion probability ($\mu = 0.1$ s) and fBm with sub-diffusive ($H = 0.1$), super-diffusive ($H = 0.9$) and purely Brownian dynamics ($H = 0.5$), together with the fitting curve and obtained scaling exponent α (intervals longer than 0.1 s; dashed magenta line indicates fitting curve; estimated values of α are shown on the graph; Fig. 2*C*). To obtain the cleanest form of the relationship between H and α we also applied the fitting approach to histograms generated using only T_{diff} values (the same used for the T_{res} series; the result of these fittings and the histograms are shown in Fig. 3*A*). The numerical α values obtained with this analysis (Table 1) are in line with the theoretically predicted ones ($\alpha = H - 2$) (Ding & Yang, 1995) and α is inversely proportional to the Hurst index as expected,
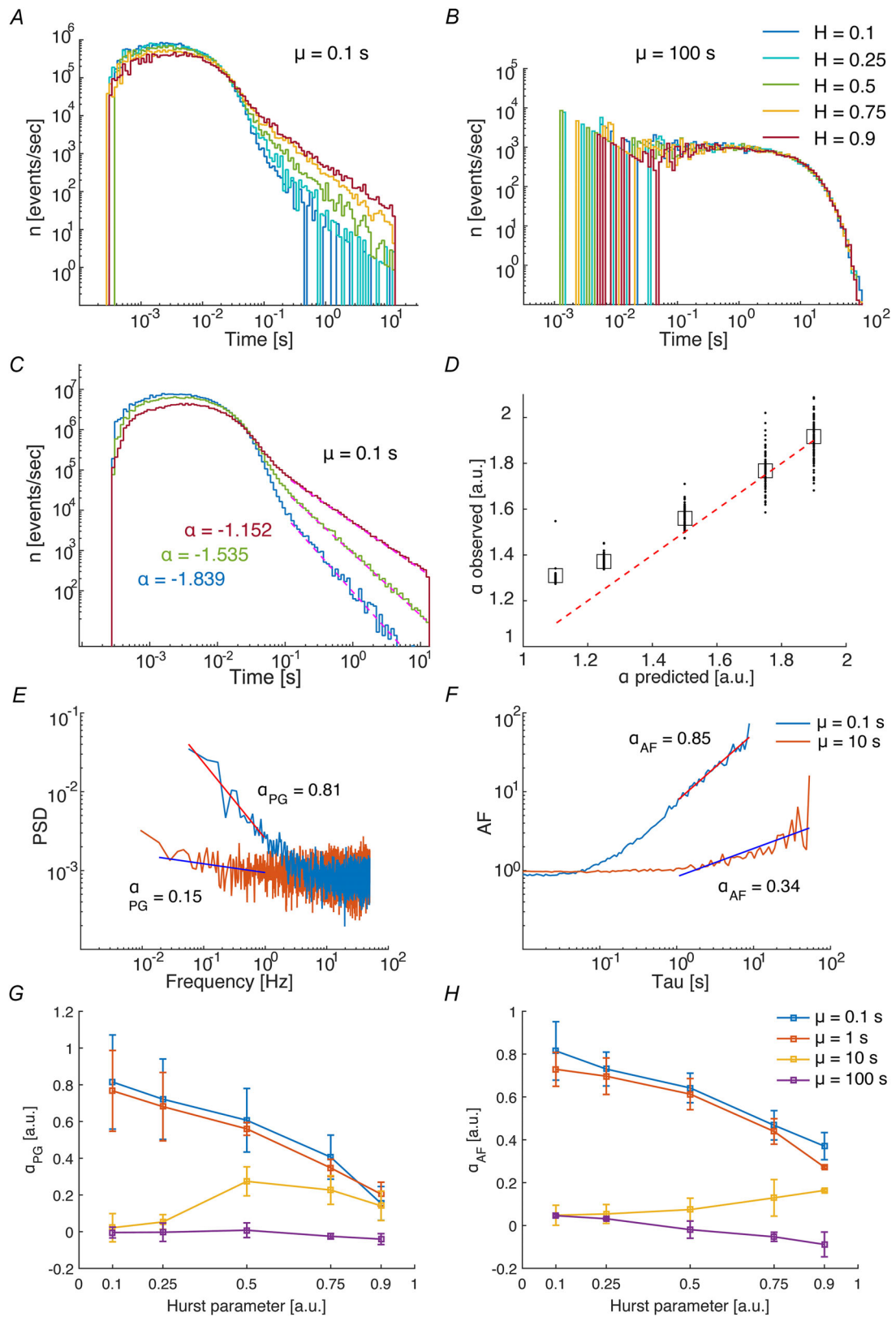
Figure 2. Analysis of simulated series of single vesicle fusion with fBm dynamics

A and *B*, log-binned histograms of T_{rel} series with $H = 0.1$–0.9 and $\mu = 0.1$ s (*A*) or 100 s (*B*). *C*, three exemplar histograms ($H = 0.1, 0.5, 0.9$; $\mu = 0.1$ s) with linear fitting for intervals longer than 0.1 s (dashed magenta lines) of the scaling exponent α (estimated values are shown on the graph). *D*, relationship between predicted (as a

function of H) and estimated values of α (fitting on log-binned histograms of T_{diff} series; $n = 100$ series simulated for each value of H). E and F, exemplar graphs of periodogram (E) and Allan factor (F) analysis on T_{rel} series with $\mu = 0.1$ (blue) and 10 s (orange) and $H = 0.1$; both methods were employed to quantify the fractal or power-law behaviour (straight lines indicate fitting range). G and H, values of the fractal exponent estimated using periodogram (α_{PG}; G) or Allan factor (α_{AF}; H) from 100 simulated T_{rel} series with all tested combinations of H (0.1, 0.25, 0.5, 0.75, 0.9) and μ (0.1, 1, 10, 100). Each simulated T_{rel} series included 10,000 fusion events where the T_{diff} value was obtained from a fBm with 100,000 samples (data shown as means $\pm$ SD). [Colour figure can be viewed at wileyonlinelibrary.com]

but there is a ceiling effect for H values close to 0.9 (super-diffusive regime) (Fig. 2D). By comparing the results of α fitting on T_{rel} and T_{diff} histograms, we can conclude that in the former case the estimated α values are in line with the predicted ones for all the three forms of diffusion, at least when the fusion process T_{fus} is fast ($\mu = 0.1$ s), i.e. the exponential component of the distribution does not excessively mask the heavy tail (Fig. 2B).

From these simulations we can predict that the motion dynamics of the vesicle before it docks to the presynaptic membrane can affect the output release series, thus representing a potential source for power-law and fractal characteristics broadly found in neuronal signalling. In addition, the interval distributions produced are in line with the deviance from a Poisson process that has been previously observed at single synaptic boutons (Abenavoli et al., 2000; Forti et al., 1997; Lamanna et al., 2011, 2012). Importantly, if fusion probability is sufficiently high, also the diffusive properties of the presynaptic milieu and the directed/undirected motion features of the vesicle might be well estimated by fitting the scaling exponent of the interval histogram. The variability in diffusion regimes and fusion probabilities between different synaptic boutons might be one of the reasons why quantal release interval distributions have been fitted using different approaches over time (e.g. with mono, bi- and multi-exponential functions (Abenavoli et al., 2002; Lamanna et al., 2011, 2012), gamma distribution (Lowen et al., 1997), etc.).

We then proceeded to verify if the inclusion of vesicle motion dynamics in our spontaneous neuro-transmission model not only produces power-law features and deviation from Poisson interval distributions, but also power-law/fractal characteristics in quantal release time series (Lamanna et al., 2015; Lowen et al., 1997). In addition, we wondered how fusion probability (μ) would impact the detection and quantification of these fractal features. PG and the AF methods were applied to the same T_{res} series analysed above. A linear scaling was applied to time series in order to get comparable time scales and the frequency ranges among different simulations (of H and μ). Figure 2E and F show exemplar graphs of PG and AF analyses, respectively, which were performed on a simulation with the same $H = 0.1$ and low ($\mu = 10$ s, red line) or high ($\mu = 0.1$ s) fusion probabilities. As

can be appreciated from these graphs, the value of the estimated fractal exponent α is comparable between the two methods and approaches the predicted one for these measures ($\alpha_{\text{PG}} = \alpha_{\text{AF}} = 1 - H$) (Lowen & Teich, 2005). Nevertheless, when fusion probability is lower ($\mu = 10$ s), the obtained value of α is strongly decreased, suggesting that the final step of fusion masks fractal features in quantal release series, similarly to what occurs for interval distributions (see above). Both the comparability of the two methods and the dampening effects of lower fusion probabilities can be well appreciated by looking at the graphs in Fig. 2G and H, where the results of PG and AF analyses are shown, respectively, for all the investigated combinations of H and μ (numerical results are provided in Tables 2 and 3. Mean and standard error of the estimated α value (for each method) are computed over $n = 100$ realizations of the simulation process (T_{res} series). From these results it can also be appreciated that the dampening effect of mid-range fusion probability ($\mu = 10$ s, yellow line in Fig. 2G and H) is lower for BM and super-diffusive regimes ($H \geq 0.5$), while fractal features are totally lost at $\mu = 100$ s.

Graphs showing periodogram and Allan factor analyses, similar to the ones shown in Fig. 2E and F, but for all the other combinations of simulation parameters, are shown in Fig. 3B and C, respectively.

Simulations of spontaneous release series involving independent vesicles with uniform or different motion dynamics

We were then interested in evaluating whether the results described above can be obtained also when a significant number of vesicles participate simultaneously to the release process. At first, we superimposed the simulated release events form $n = 20$ vesicles to produce a final series of T_{res}. We can imagine that such series is produced by vesicles recycling at the same fusion site, active zone or synapse, but also vesicles that fuse at different synaptic boutons targeting the same postsynaptic neuron (producing a unique series of quantal discharges that is generally obtained with whole-cell patch clamp configurations), as these can be reasonably supposed to act independently from each other at least under spontaneous fusion conditions. In our first analysis both H and μ were kept fixed for all vesicles, and hence, based
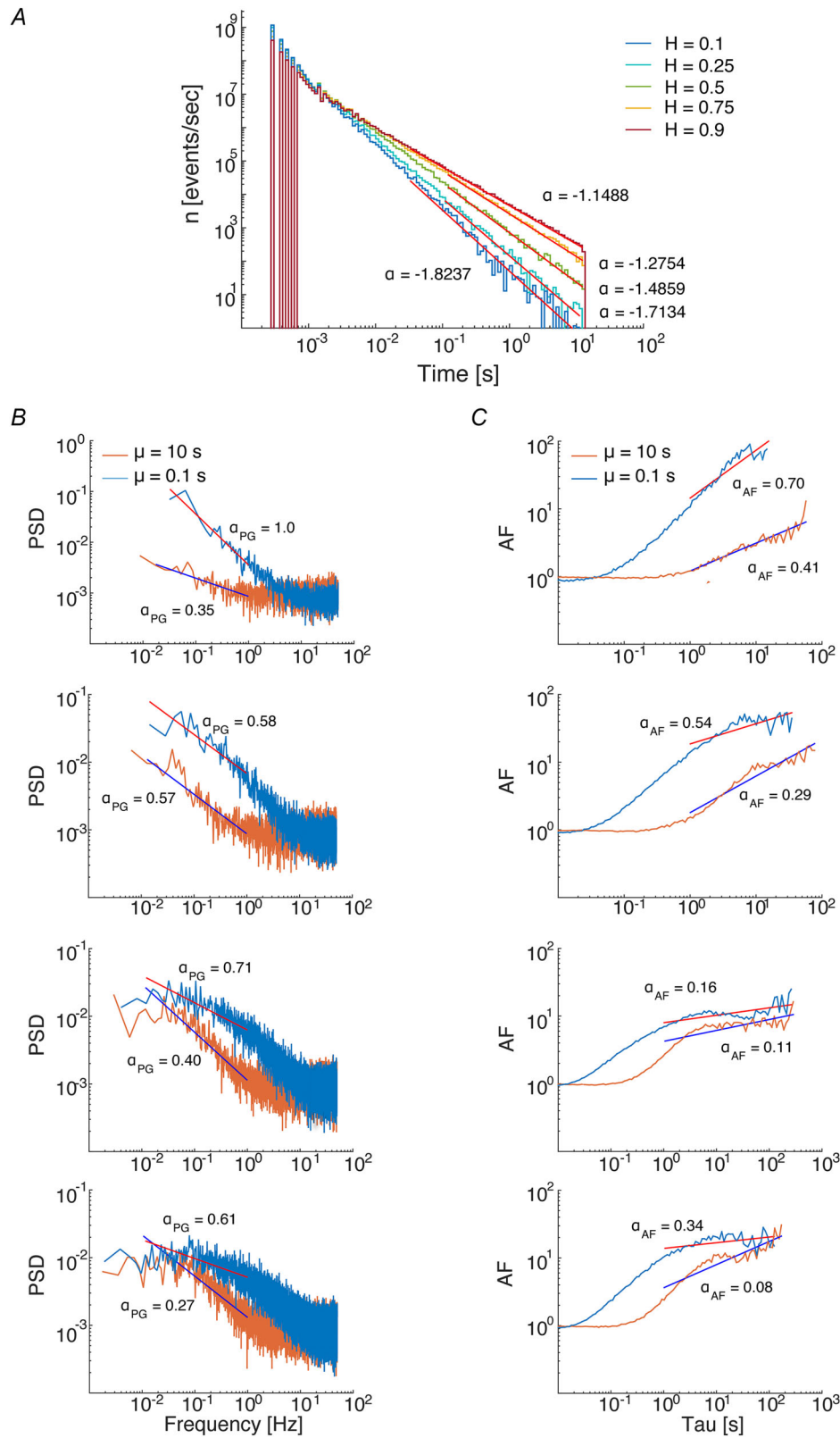
Figure 3. Fitting power-law and fractal behaviours using interval distribution, periodogram and Allan factor

A, log-binned histograms of the diffusion time series (T_{diff}) generated using fBm with different values of H (0.1, 0.25, 0.5, 0.75, 0.9) and estimation of the scaling exponent α of the power-law characterizing the distribution's

tail. *B* and *C*, periodogram (*B*) and Allan factor (*C*) analyses are shown for several combinations of *H* (one value for each row from top to bottom: 0.25, 0.5, 0.75, 0.9; see Fig. 2*E* and *F* for *H* = 0.1) and μ (0.1, 10; same graph). Straight lines represent the fitting of the power-law function to estimate the scaling exponent (α_{PG}, α_{AF}). [Colour figure can be viewed at wileyonlinelibrary.com]

Table 2. Numerical results (mean ± SD) of fractal exponent α_{PG} estimations via PG

Hurst parameter	μ = 0.1 s	μ = 1 s	μ = 10 s	μ = 100 s
0.1	0.81 (± 0.256)	0.76 (± 0.220)	0.02 (± 0.077)	−0.004 (± 0.029)
0.25	0.72 (± 0.219)	0.68 (± 0.186)	0.05 (± 0.040)	−0.003 (± 0.050)
0.5	0.60 (± 0.173)	0.56 (± 0.035)	0.27 (± 0.079)	0.008 (± 0.040)
0.75	0.40 (± 0.120)	0.34 (± 0.047)	0.22 (± 0.078)	−0.02 (± 0.015)
0.9	0.15 (± 0.092)	0.20 (± 0.065)	0.14 (± 0.080)	−0.04 (± 0.030)

The observed values were obtained from 100 simulations (100,000 fBm samples for a maximum of 10,000 fusion events) of one single vesicle for the selected Hurst parameter and different values of μ.

Table 3. Numerical results (mean ± SD) of fractal exponent α_{AF} estimations via AF

Hurst parameter	μ = 0.1 s	μ = 1 s	μ = 10 s	μ = 100 s
0.1	0.81 (± 0.136)	0.72 (± 0.079)	0.04 (± 0.047)	0.04 (± 0.002)
0.25	0.73 (± 0.079)	0.69 (± 0.085)	0.05 (± 0.044)	0.03 (± 0.001)
0.5	0.64 (± 0.068)	0.61 (± 0.072)	0.07 (± 0.053)	−0.01 (± 0.041)
0.75	0.46 (± 0.066)	0.43 (± 0.059)	0.12 (± 0.085)	−0.05 (± 0.021)
0.9	0.37 (± 0.063)	0.27 (± 0.01)	0.16 (± 0.01)	−0.08 (± 0.057)

The observed values were obtained from 100 simulations (100,000 fBm samples for a maximum of 10,000 fusion events) for the selected Hurst parameter and different values of μ.

on the previous considerations, these can be reasonably assumed located in the same presynaptic environment and recycling through the same release machinery, but also recycling at different synaptic boutons with the same diffusive properties and fusion probabilities (a much more unlikely case). All the T_{res} series produced at this stage were linearly scaled as discussed above to facilitate comparisons.

Log-binned histograms from these series for μ = 0.1 s and *H* = 0.1–0.9 are shown in Fig. 4*A*. From these graphs, it is still possible to appreciate power-law behaviour at the interval distribution's tail, with a slope steepness that reduces when passing from a sub-diffusive to a super-diffusive regime, similarly to what was observed for simulations involving a single vesicle. Figures 3*C* and 4*B* show the PG and AF analyses performed on these series, respectively. The results of fractal analysis provide us with trends which are very close to the ones shown in Fig. 2*G* and *H*, although the steepness of the curves relating the values of *H* and estimated α is much lower, indicating a different underlying relationship between the two parameters in these conditions. Such an effect is slightly lower for the AF method. As noticed for a

single vesicle series, the reduction of fusion probability strongly dampens the fractal exponents, but this effect is weaker than previously observed and, more importantly, seems independent from the diffusion regime and method adopted. Furthermore, in order to qualitatively evaluate the effects of having strongly heterogeneous vesicle pools contributing to the same release process, we generated series of fusion events by mixing two pools with either different diffusion properties or different fusion probabilities.

As for the former case, Fig. 4*D* shows log-binned histograms obtained with high fusion probability (μ = 0.1 s) and different combinations of *H* for the two vesicle pools (*n* = 10 vesicles for each pool; green: *H* = 0.1 and 0.5; blue: *H* = 0.1 and 0.9; red: *H* = 0.5 and 0.9): by comparing Fig. 4*D* with Fig. 4*A*, we can state that the power-law tail of the interval distribution obtained with two different *H* values looks very similar to the one obtained with a single pool with an average *H* (e.g. the mix *H* = 0.1 and 0.5 looks similar to *H* = 0.25 ≅ 0.3). On the other hand, when we analysed the interval histograms of the T_{rel} series with the same combinations of *H* but low release probability (μ = 10 s), the power-law behaviour

produced results that were homogeneous among all mixed simulations (Fig. 4*E*). In other words, we might argue that when fusion probability is high, power-law behaviour observed in experimental spontaneous release series can still emerge from the diffusion dynamics of many vesicles from synapses targeting the same postsynaptic neuron. Nevertheless, we can also predict that the more synaptic sites with sub-diffusive or Brownian diffusion properties contribute to the overall process, the less steep and differentiable those power-law tails will appear in interval distributions. Interestingly, as it is shown by histograms in Fig. 4*F*, when the two pools mixed have the same fBm properties (blue: $H = 0.1$; green: $H = 0.5$; red: $H = 0.9$) but both fast and slow fusion kinetics ($\mu = 0.1$ and 10 s for the two pools, respectively), the power-law tails are clearly visible and differentiable. Thus, power-law features are likely to be well detected in experimental series provided that a significant fraction of the vesicles involved fuse with high probability.

Experimental and predicted distributions of distances from the active zone for vesicle with a recent history of exocytosis

In order to evaluate the consistency of our diffusion-based model with the real dynamics of vesicle motion, we conducted ultrastructural analysis of recycling vesicles at central synaptic boutons. Vesicles actively involved in endo–exocytotic cycles were stained using horseradish peroxidase uptake during field electrical stimulation (0.5 Hz for 10 min; 300 stimuli; 20 mV/cm). Electron microscopy image stacks (6 images per stack) were acquired to identify all stained vesicles from single synaptic boutons. The acquisition procedure allowed us to obtain horizontal sections of the bouton where the presynaptic membrane could be always clearly identified as a line (juxtaposed to an electron dense postsynaptic region), with a more electron dense region reminiscent of the active zone (AZ). For each vesicle in each section (red dots in Fig. 5*A* and *B*), we measured the minimum
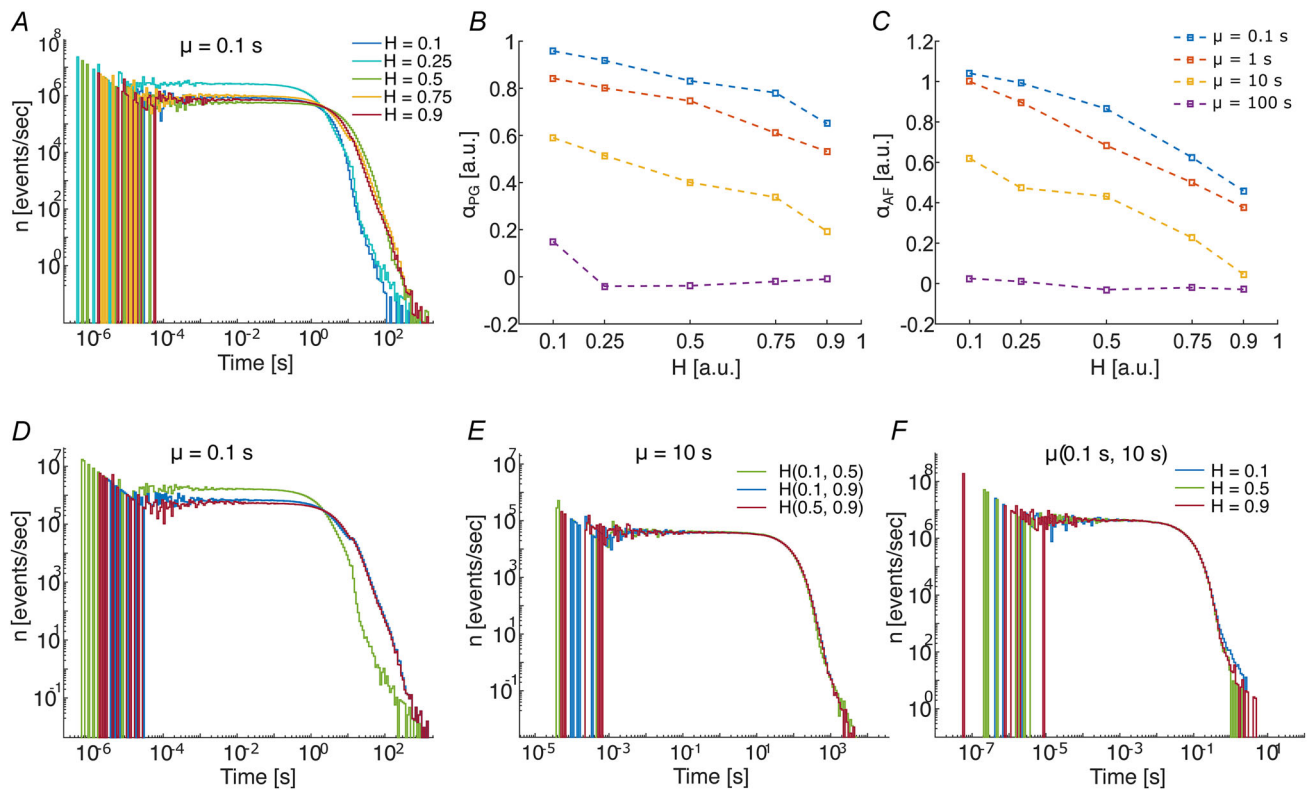

Figure 4. Analysis of simulated series of multiple vesicles' fusion with homogeneous or heterogeneous diffusive properties and fusion probabilities

A, log-binned histograms of T_{rel} fusion series generated by $n = 20$ vesicles undergoing fBm diffusion with homogeneous H (range 0.1–0.9) and the same fusion probability $\mu = 0.1$ s. *B* and *C*, values of the fractal exponent estimated using periodogram (α_{PG}; *B*) or Allan factor (α_{AF}; *H*) from T_{rel} series generated by a homogeneous pool of $n = 20$ vesicles for all tested combinations of H (0.1, 0.25, 0.5, 0.75, 0.9) and μ (0.1, 1, 10, 100). *D*–*F*, exemplar log-binned histograms of T_{rel} fusion series generated by two pools of vesicles ($n = 10$ vesicles for each pool) with heterogeneous properties: different values of H (green: $H = 0.1$ and 0.5; blue: $H = 0.1$ and 0.9; red: $H = 0.5$ and 0.9) and same fusion probability ($\mu = 0.1$ s, *D*; $\mu = 10$ s, *E*); different values of fusion probability ($\mu = 0.1$ and 10 s) and same value of H (blue: $H = 0.1$; green: $H = 0.5$; red: $H = 0.9$) (*F*). [Colour figure can be viewed at wileyonlinelibrary.com]

distance (yellow dashed line) from the whole presynaptic membrane (purple dashed line; Fig. 5*A*) and from the AZ (green dashed line; Fig. 5*B*) separately, on the section plane. An exemplar histogram of synaptic vesicle distances obtained from a single synapse is shown in Fig. 5*C* (*n* = 44 vesicles; distance from cleft = 236 ± 170 nm, left plot; distance from AZ = 245 ± 167 nm; mean ± SD, right plot; Fig. 5*C*). The histograms for pooled data are shown in Fig. 5*D* (*n* = 98 vesicles from 3 boutons; distance from cleft = 176 ± 145 nm, left plot; distance from AZ = 185 ± 146 nm, right plot; mean ± SD; Fig. 5*D*). The pooled histogram suggests that the underlying distribution is right-skewed, with a slow decaying right tail.

To make a comparison between real distances and our model's predictions, we simulated the flight of 100 vesicles with the same diffusion properties (fBm with
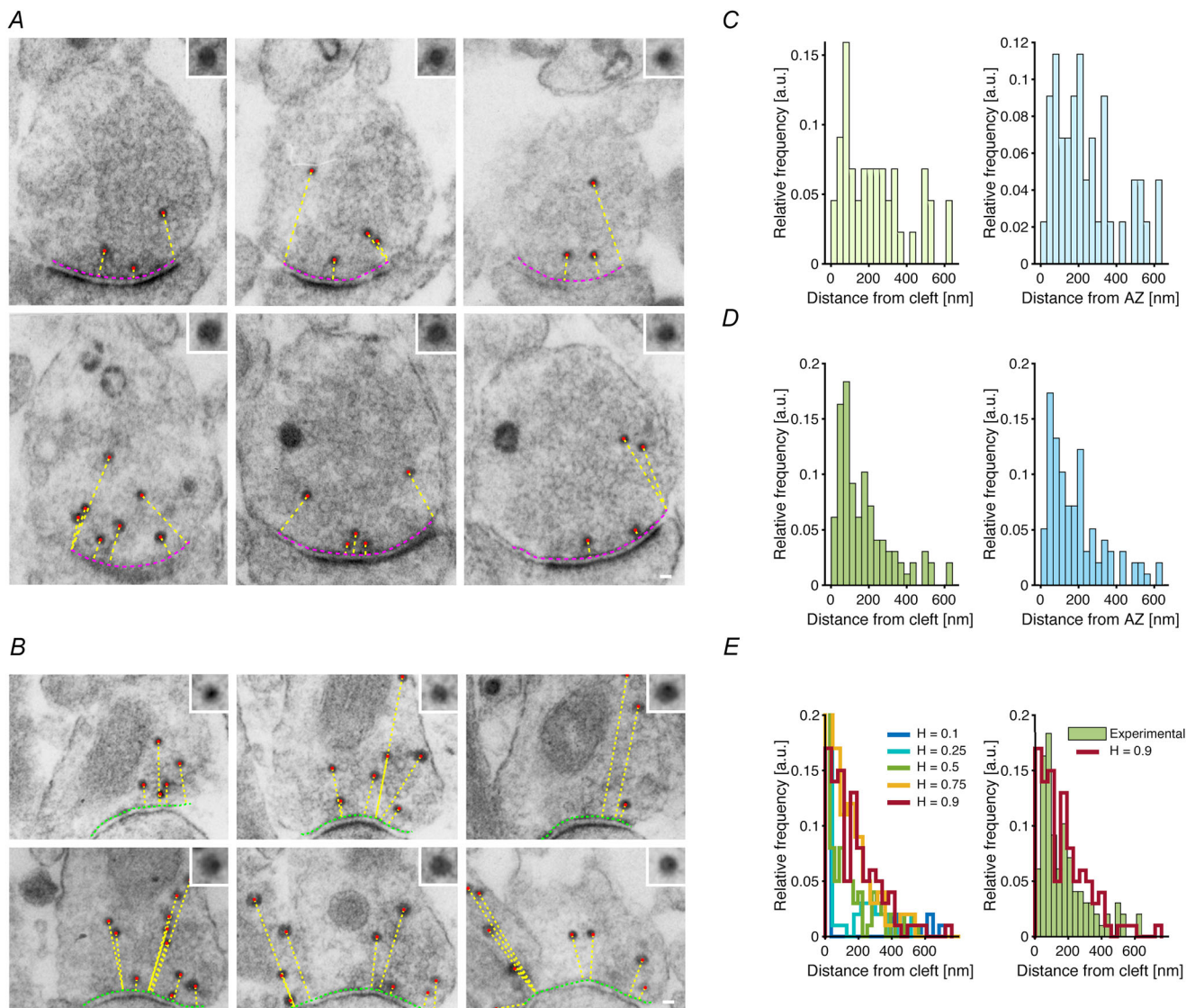
Figure 5. Experimental and predicted distributions of distances from the active zone for vesicle with a recent history of exocytosis

A and *B*, serial electron microscopy images showing parallel sections of central synaptic boutons. Vesicles (red dots) were stained using HRP (10 mg/ml) uptake during field electrical stimulation (10 min; 0.5 Hz; 20 mV/cm) of cultured hippocampal neurons (fixed with 4 % paraformaldehyde). Vesicles' minimum distance (yellow dashed line) from presynaptic membrane (purple dashed line; *A*) and active zone (AZ; *B*) was measured on each section (bar = 50 nm). *C* and *D*, histograms of vesicles distance from cleft (pale green, left plot) and AZ (pale blue, right plot) are shown for an exemplar synaptic bouton (*C*) and for pooled data (*n* = 98 vesicles from 3 boutons; *D*). *E*, histograms of vesicles distance for different diffusive regimes (fBm with *H* = 0.1–0.9; left plot) simulated in the same experimental conditions described above (0.5 Hz stimulation, 10 min). Right plot provides a comparison between the pooled vesicle distances from the experimental boutons (green) and the best-fitting histogram from simulations (*H* = 0.9). [Colour figure can be viewed at wileyonlinelibrary.com]

$H = 0.1–0.9$), assuming that each vesicle fused at least once during the stimulation epoch (the first fusion time was randomly selected from the 300 stimulation times in a 10 min epoch). If the vesicle flight ends at the presynaptic membrane ($x = 0$) before one of the remaining stimuli, then it fuses again with $p = 1$ at the next stimulus time and a new flight is simulated (if the vesicle reaches $x = 0$ after the last stimulus, that will be the final position). The final distance of all vesicles from presynaptic membrane ($x = 0$) is computed at the end of the epoch and the related histogram is shown in Fig. 5*E* (left plot) with different colour for different values of H. We then compared these simulation histograms with the experimental one (pooled vesicles) and identified the more similar one (minimum mean square error), the one generated with $H = 0.9$ (Fig. 5*E*, right plot). As can be appreciated by looking at the superimposition of the two histograms in Fig. 5*E*, our simulation provides a very good prediction (in shape) of real vesicles distance data and suggests that, at least for these synapses, a super-diffusive regime is met, which might be related to molecular motors involved in the motion dynamics of vesicles involved in action potential evoked endo–exocytosis (Peng et al., 2012).

Fitting the diffusion-based model of spontaneous release with electrophysiological recordings from single synaptic boutons

In order to directly test the performance of our model in describing the dynamics of real spontaneous release, we collected and analysed quantal release series gathered using the loose-patch (LP) recording technique (Forti et al., 1997). Figure 6*A* shows a scheme of the recording technique. Synaptic boutons are visually identified using a fluorescent probe (FM-1-43 or eGFP-SynaptoZip), then electrically isolated in the tip of the pipette by applying mild suction. Figure 6*B* shows exemplar traces of a LP recording (inward currents are positive as it is an extracellular recording). Such recordings still provide the finest and lowest scale information, which is currently achievable with high temporal precision, about quantal release dynamics. Indeed, real-time super-resolution imaging approaches still cannot provide precise information about the time of release. Nevertheless, based on this approach, we cannot distinguish between the fusion times of different vesicles in the same bouton.

For this reason, we will assume that either (1) most fusion times are generated by the same vesicle during a recording epoch or (2) vesicles alternate in their fusion activity but have very similar diffusional properties, as well as similar fusion probabilities. The second possibility is much more likely since the presynaptic environment, including the AZ and the fusion machinery, is shared (and it is generally assumed in quantal analysis models). As we showed before (Fig. 4), our model produces similar features of the release series in terms of interval distributions, PG and AF, even when $n = 20$ vesicles independently contribute to the process. Thus, we can reasonably test the performance of our modelling approach on LP series. To achieve this aim, we developed a custom data fitting approach.

At first, we fitted the power-law heavy-tail, if present, using a linear fitting of the log-binned histogram for intervals longer than 1 s, which provides the power-law exponent α. In Fig. 6*C*–*E*, the log-binned histograms from three exemplar recordings are shown together with the fitting of the α (blue line). These recordings are reminiscent of the three canonical diffusive regimes: super-diffusive ($\alpha = -1.09$; Fig. 6*C*), Brownian motion ($\alpha = -1.51$; Fig. 6*D*) and sub-diffusive ($\alpha = -1.66$; Fig. 6*E*). Above each histogram, the time course of release events from the related recording is shown. Importantly, all the $n = 17$ recordings analysed show a clear power law in the distribution tail which can be easily fitted on the log-binned histogram. This result indicates that our model captures an important (always present) feature of the release process which is not predicted by the other modelling approaches, such as mono- or hyper-exponential models.

The exemplar recording whose time course and log-binned interval histogram are show in in Figs 5*I* and 6*F*, respectively, will be used to describe the successive steps of our fitting algorithm. We estimated λ_1, λ_2, the parameters that in our model describe fusion and endocytosis timings, respectively, using the hypo-exponential pdf of eqn (5), applied to intervals lower than the cutoff of 1 s (red line in Fig. 6*I*). Starting from λ_1, λ_2, and α ($H = \alpha + 2$), we were thus able to simulate a release series using our computational model based on fBm as above. The time course and the log-binned histogram of the simulated series are shown in Figs 5*J* and 6*G*, respectively, together with α fitting. The results are appreciably good. Then, we obtained a numerical solution of the convolution between eqn (5) and a generalization of eqn (6), where the power-law exponent was changed from -1.5 (Lévy distribution) to a generic α. Although this is an approximated solution of the final pdf of our model, it seems reasonable for modelling first return times of fBm at long intervals (Rangarajan & Ding, 2000; Sornette, 2006). We then fitted this pdf to our data using maximum likelihood estimation (mle) and imposing fixed values of λ_1, λ_2 and α, which guaranteed convergence of the mle algorithm. This allowed us to obtain an estimate of C and then of the diffusion constant D. We then obtained a simulated series from the full model (λ_1, λ_2, α and C parameters) using Monte Carlo sampling: the time course and the log-binned interval histogram of this simulation are shown in Fig. 6*K*, together with the numerical pdf
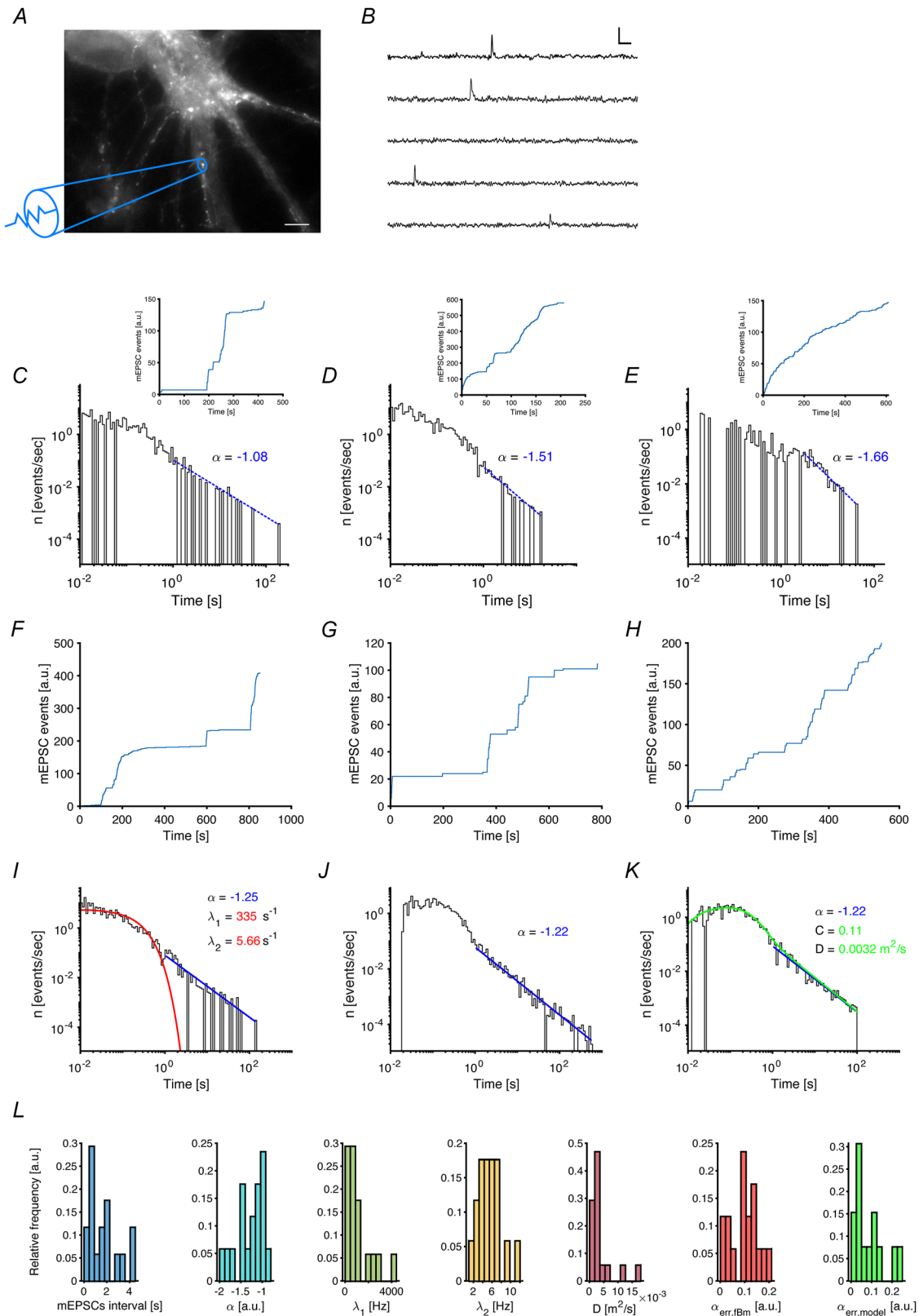
Figure 6. Analysis of electrophysiological recordings from single synaptic boutons

A, scheme of the recording technique. Synaptic boutons are visually identified using a fluorescent probe (eGFP-SynaptoZip fluorescence in white; bar = 5 μm), then electrically isolated in the tip of the pipette (blue) by applying mild suction. *B*, exemplar current traces showing a few mEPSCs. *C–E*, exemplar log-binned histograms of mEPSCs interval distributions from three recordings with different values of α (fitted by the blue line) reminiscent

of the three diffusive regimes: super-diffusive ($\alpha = -1.09$; *C*), Brownian motion ($\alpha = -1.51$; *D*) and sub-diffusive ($\alpha = -1.66$; *E*). Above each histogram, the time-course of release events from the related recording is shown. *F–K*, an exemplar experiment is analysed and fitted using the diffusion-based model. Time-courses are shown for the real series (*F*), a series simulated with the fBm algorithm (*G*), and a series simulated using a numerical solution of the diffusion-based model pdf (*H*; see text for details). Log-binned histograms of the series in *F*, *G* and *H* are shown in *I*, *J*, and *K*, respectively, together with fitting curves: hypo-exponential model (eqn (5); red line; λ_1 and λ_2; *I*); power-law heavy tail (blue, α; *I–K*); diffusion-based model pdf (green; *C* and *D* parameters). *L*, histograms showing the frequency distribution of the estimated parameters for all recordings, from left to right: average inter-mini interval, α, λ_1, λ_2, *D*, error in α when simulated using fBm ($\alpha_{\text{err,fBm}}$) and the diffusion-based model ($\alpha_{\text{err,model}}$). [Colour figure can be viewed at wileyonlinelibrary.com]

(green line). Beside increasing the qualitative goodness of the simulation, this step provided us with an estimation of the diffusion constant based on our model and the mEPSCs data, which represents a very interesting tool. However, direct validation of this approach will require simultaneous loose-patch recordings and single vesicle tracking using real-time super-resolution microscopy, a very challenging task. Histograms in Fig. 6*L* show the frequency distribution of the estimated parameters for all recordings, including α, λ_1, λ_2, *D*, as well as the computed errors in α when the release series is simulated using fBm ($\alpha_{\text{err,fBm}}$) and the diffusion-based model ($\alpha_{\text{err,model}}$). These latter indices suggest that the simulation approach based on the full model pdf (i.e. without generation of fBm flight series) might be less biased in terms of reproduction of the power-law heavy-tail.

Effects of vesicle diffusion dynamics on action potential evoked release based on a dynamic readily releasable pool

We next decided to investigate whether the diffusion dynamics of synaptic vesicles occurring before they dock to the presynaptic membrane can affect the process of evoked release as well. We can assume that whenever an action potential reaches the presynaptic bouton and the active site of release, a fraction of the recycling vesicles will be found docked and ready to be released (the so-called readily releasable pool, RRP). Based on the considerations discussed at the very beginning of this article, we argued that the RRP can increase over time due to diffusive vesicle motions that lead to their docking to the AZ or can be reduced by spontaneous vesicle fusions. The processes of molecular priming that are supposed to occur between docking and maturation of the vesicle in the RRP will be neglected here because, besides being still debated, they are thought to be very fast, in the order of milliseconds (and promoted by calcium entrance) (Neher & Brose, 2018; Silva et al., 2021), and thus much faster than the diffusion/release dynamics modelled here and the stimulation frequency that will be adopted (0.5 Hz). The same reasoning can be applied to the possible loose state of the docking process that is supposed to allow the random undocking of vesicles (Neher & Brose, 2018).

Based on these assumptions, in order to simulate evoked fusion, we exploited a dataset of spontaneous release series generated by the recycling process of $n = 20$ vesicles, with three different values of mean spontaneous fusion time (T_{fuse}; $\mu = 0.1, 1, 10$ s), and five different values of the Hurst exponent for the fBm ($H = 0.1, 0.25, 0.5, 0.75, 0.9$). We then computed the putative RRP every 2 s, which is the action potential stimulation period ($S_{\text{tim}} = 2$ s): RRP increases by 1 unit whenever a vesicle docks to the membrane after its fBm diffusion, while it decreases by 1 unit after a vesicle spontaneously fuses. The resulting time-varying RRP (named tRRP) will oscillate around an average value, and these oscillations are likely to reflect the power-law features of the fBm. We then generated evoked release series with different evoked fusion probability ($p = 0.25, 0.5, 0.75$) by using three different approaches: (1) a standard binomial model where *n* was set as the average tRRP; (2) an instantaneous binomial model where *N* was equal to tRRP at the time of evoked release; and (3) a direct fusion process where the number of released vesicles equals tRRP, i.e. the same as setting $p = 1$. The latter aims at modelling a hypothetical condition where all the variability in quantal output is ascribed to the temporal dynamics of the diffusion process: we wondered whether such a model would be able to produce quantal analysis results close to the ones produced by a classical binomial model, providing specific characteristics of the fBm.

Figures 7–9 show the results of these simulations through histograms displaying the frequency of evoked transmission events for different numbers of vesicles successfully released from the RRP. The three approaches adopted are shown with different bars colours to facilitate comparisons (blue: binomial model with *N* equal to average RRP; green: binomial model with *N* equal to tRRP; yellow: direct fusion of all tRRP vesicles). Fig. 7 shows the simulation results for the tRRP generated by a sub-diffusive regime of motion and spontaneous release (fBm with Hurst exponent $H = 0.1$), with varying *p* (column of the panel) and μ values (row of the panel). For such a diffusive regime, which is very confined, increasing μ tends to saturate the RRP so that with $\mu = 10$ s all recycling vesicles are available for evoked release. For this reason, the binomial output almost coincides between the instantaneous and the average RRP cases for $\mu = 1$ and 10 s (Fig. 7*D–I*). Nevertheless, when

$\mu = 0.1$ s a certain degree of mismatch between average and instantaneous RRP binomials can be appreciated, supporting the idea that the underlying diffusion and spontaneous release process can significantly affect evoked synaptic transmission (Fig. 7A–C). Interestingly, the histograms obtained in the latter case tend to be very similar to the one obtained with 'direct' fusion (i.e. without binomial model), in terms of mean, variance and skewness of the distribution, especially for $p = 0.75$ (Fig. 7C), thus supporting the view that binomial variability might be ascribed only to variability in RRP size, and that this can account for the level of evoked release probability. Figure 8 shows the simulation results for the tRRP generated by a Brownian motion and spontaneous release model (fBm with Hurst exponent $H = 0.5$), with varying p and μ

values. In this case, saturation is limited to $\mu = 10$ s (Fig. 8G–I). Interestingly, Brownian dynamics seem to be much more effective (compared to sub-diffusive ones) in modulating the distribution of evoked release in all cases (leading to more variability between average and instantaneous RRP binomials), and this is particularly appreciable for the lowest μ value (0.1 s). For these simulations it is even more clear that variability in evoked release output could be well modelled by the dynamic RRP, especially for $P > 0.5$ and $\mu = 0.1$ and 1 s (Fig. 8B–F), e.g. for a broader range of physiological cases. Figure 8 shows the simulation results for the tRRP generated by a super-diffusive regime of motion and spontaneous release (fBm with Hurst exponent $H = 0.9$), with varying p and μ values. This case appears as another extreme condition
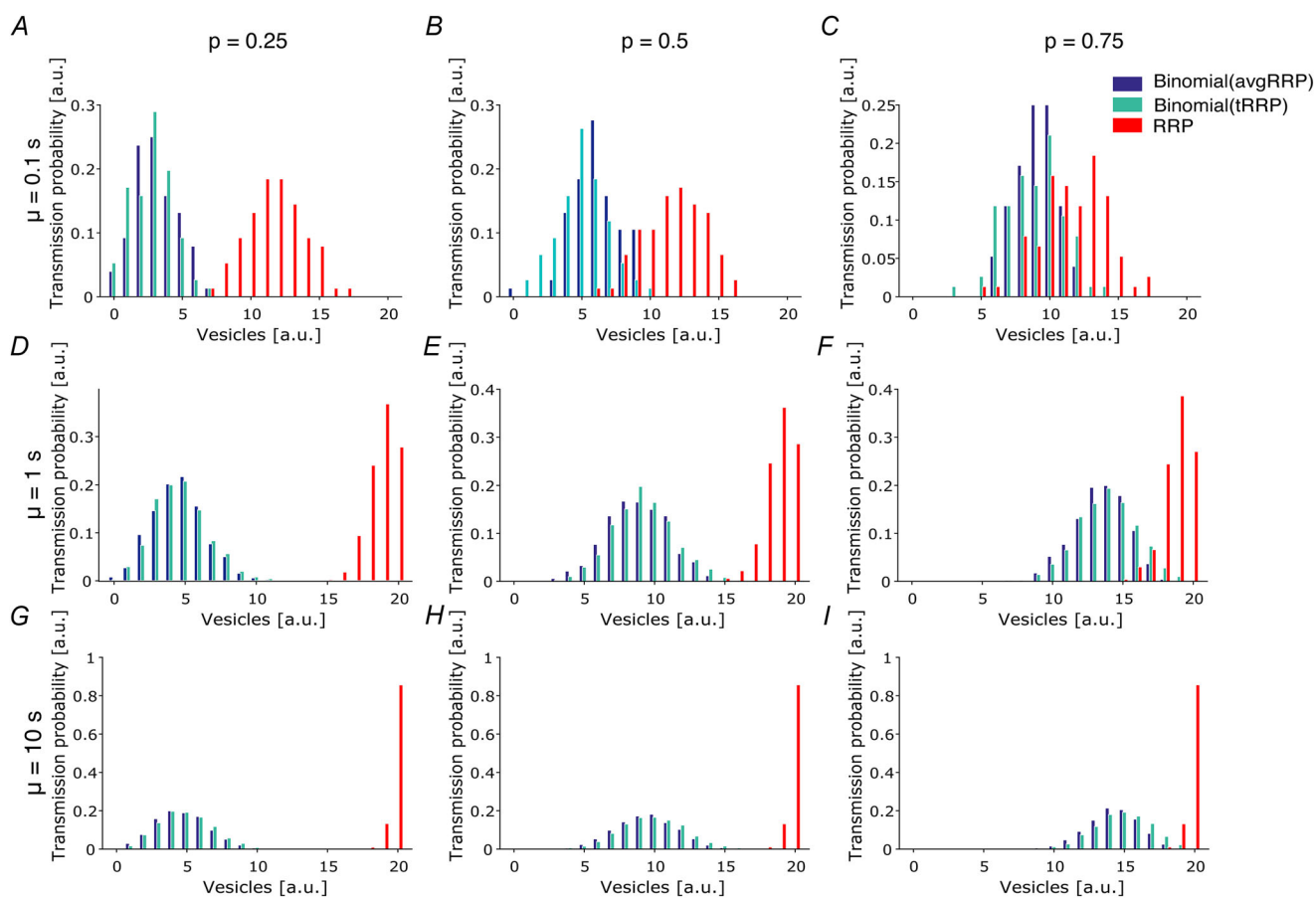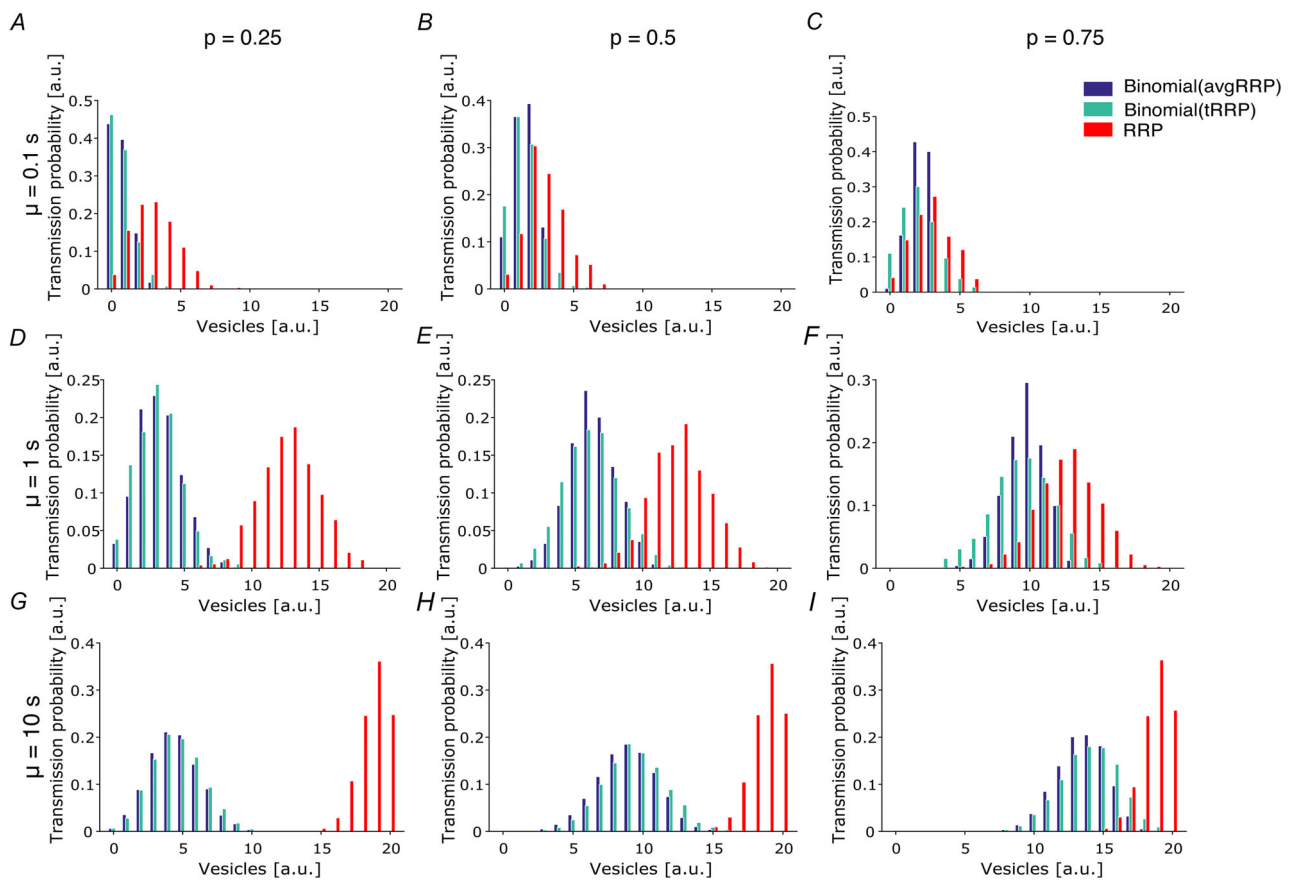

Figure 7. Analysis of simulated series of evoked vesicle fusion with dynamic RRP loaded by sub-diffusive (*H* = 0.1) vesicle motion

A–I, histograms showing the frequencies of evoked transmission events (stimulation period 2 s) with varying number of vesicles present in the RRP, whose size is regulated by sub-diffusive motion/docking of 20 vesicles (fBm with Hurst exponent *H* = 0.1) and their spontaneous fusion (see text for details). For each graph, blue bars show data from a binomial model with *N* equal to the average RRP, green bars show data from a binomial model with *N* equal to the instantaneous RRP (tRRP) and yellow bars show data from a *p* = 1 condition (fused vesicles = tRRP at stimulation time). *A–C*, simulations with mean spontaneous fusion time (*T*~fuse~) μ = 0.1 s and evoked fusion probability *p* = 0.25 (*A*), 0.5 (*B*), and 0.75 (*C*). *D–F*, simulations with mean spontaneous fusion time (*T*~fuse~) μ = 1 s and evoked fusion probability *p* = 0.25 (*D*), 0.5 (*E*), and 0.75 (*F*). *G–I*, simulations with mean spontaneous fusion time (*T*~fuse~) μ = 10 s and evoked fusion probability *p* = 0.25 (*G*), 0.5 (*H*), and 0.75 (*I*). [Colour figure can be viewed at wileyonlinelibrary.com]

in which, opposite to what is shown in Fig. 7, saturation toward an empty RRP occurs for $\mu = 0.1$ s (Fig. 7*A*–*C*). Nevertheless, reasonably, this time saturation leads to a higher impact of motion dynamics on evoked fusion: this is expected since the output is strongly limited by RRP replenishment. For most of the parameters adopted here, 'direct' fusion and binomial outputs almost perfectly overlap (e.g. Fig. 8*F*), or they could, with a shift of the mean (Fig. 8*G*–*I*). In addition, the super-diffusion case produces the strongest modulatory effect by the spontaneous release process, as it can be appreciated by comparting blue and green bars of histograms obtained with $\mu = 1$ and 10 s (Fig. 8*D*–*I*). Figures 10 and 11 show the histograms from the simulations obtained using intermediate values of the Hurst exponent $H = 0.25$ (sub-diffusive, Fig. 10) and 0.75 (super-diffusive, Fig. 11).

Discussion

In this work, we developed a probabilistic model able to simultaneously account for non-linear features and non-homogeneity of the spontaneous synaptic transmission process, based on simple biophysical assumptions and, most importantly, on the diffusion dynamics of single synaptic vesicles. To this end, we simulated a stick and diffuse process where vesicles dock to the presynaptic membrane, fuse spontaneously after an exponentially distributed interval, are endocytosed to be recycled with another exponential delay, and finally diffuse following a fractional Brownian motion in the presynaptic compartment, until they come back to the docking site (Fig. 1*A*). The use of the fBm process allowed us to model different conditions of vesicle diffusion,
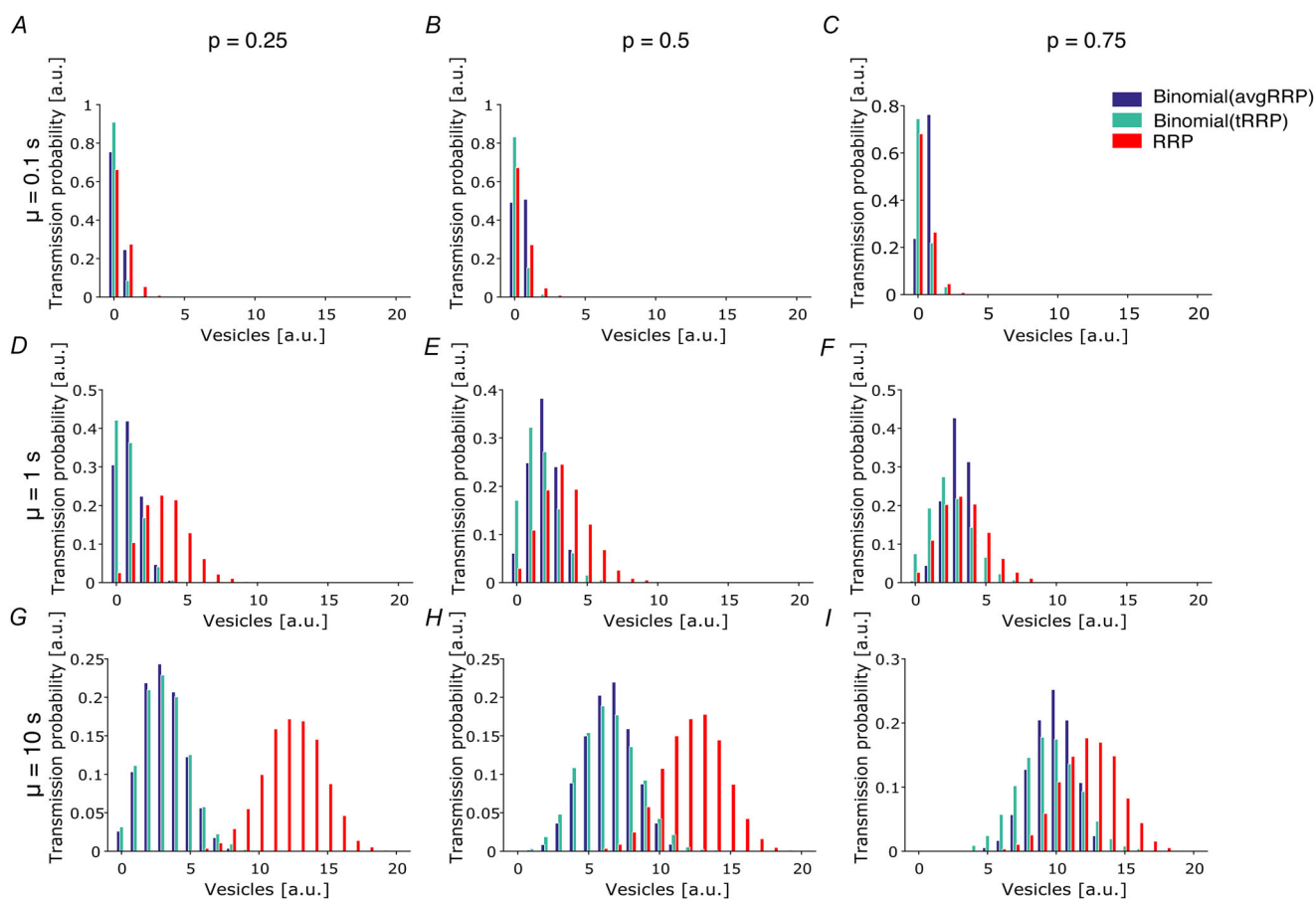

Figure 8. Analysis of simulated series of evoked vesicle fusion with dynamic RRP loaded by Brownian ($H = 0.5$) vesicle motion

A–*I*, histograms showing the frequencies of evoked transmission events (stimulation period 2 s) with varying number of vesicles present in the RRP, whose size is regulated by sub-diffusive motion/docking of 20 vesicles (fBm with Hurst exponent $H = 0.5$, i.e. Brownian motion) and their spontaneous fusion (see text for details). For each graph, blue bars show data from a binomial model with *N* equal to the average RRP, green bars show data from a binomial model with *N* equal to the instantaneous RRP (tRRP) and yellow bars show data from a $p = 1$ condition (fused vesicles = tRRP at stimulation time). *A*–*C*, simulations with mean spontaneous fusion time (T_{fuse}) $\mu = 0.1$ s and evoked fusion probability $p = 0.25$ (*A*), 0.5 (*B*), and 0.75 (*C*). *D*–*F*, simulations with mean spontaneous fusion time (T_{fuse}) $\mu = 1$ s and evoked fusion probability $p = 0.25$ (*D*), 0.5 (*E*), and 0.75 (*F*). *G*–*I*, simulations with mean spontaneous fusion time (T_{fuse}) $\mu = 10$ s and evoked fusion probability $p = 0.25$ (*G*), 0.5 (*H*), and 0.75 (*I*). [Colour figure can be viewed at wileyonlinelibrary.com]

from sub-diffusive to super-diffusive regimes, by varying Hurst exponent H (Fig. 1*B*). From the simulated series of spontaneous release, we obtained log-binned histograms that display clear deviations from the Poisson hypothesis, with evident heavy tails (Fig. 2*A*). More specifically, the resulting interval distributions seem to follow the exponential case only for shorter intervals and the heavy tail for longer ones, generating bounces at intermediate ranges. Importantly, we were able to provide an analytical derivation of the model in a closed form equation for the limit case of $H = 0.5$, i.e. Brownian motion (eqn (8); Fig. 1*D*). Such a model clearly demonstrates that the heavy tail of interval distributions and its power-law shape are produced by the diffusion process through the Lévy distribution of vesicle return times. When we super-

posed fusion events from several recycling vesicles with mixed homogeneous or heterogeneous diffusion/fusion properties (Fig. 3), the complexity of these distributions even increased. Single bouton series have been previously modelled as sums of two or three exponential components (hyper-exponential distribution) (Abenavoli et al., 2000). However, no exponential component can capture the power-law heavy tail that we observed in our electro-physiological recordings of spontaneous transmission at single synaptic boutons while our model provided superior fitting results (Fig. 6), which might be also valuable for estimating diffusion properties of the presynaptic milieu. Our ultrastructural analysis (Fig. 5) further supports the capabilities of our model in predicting the motion dynamics of vesicles undergoing fusion.
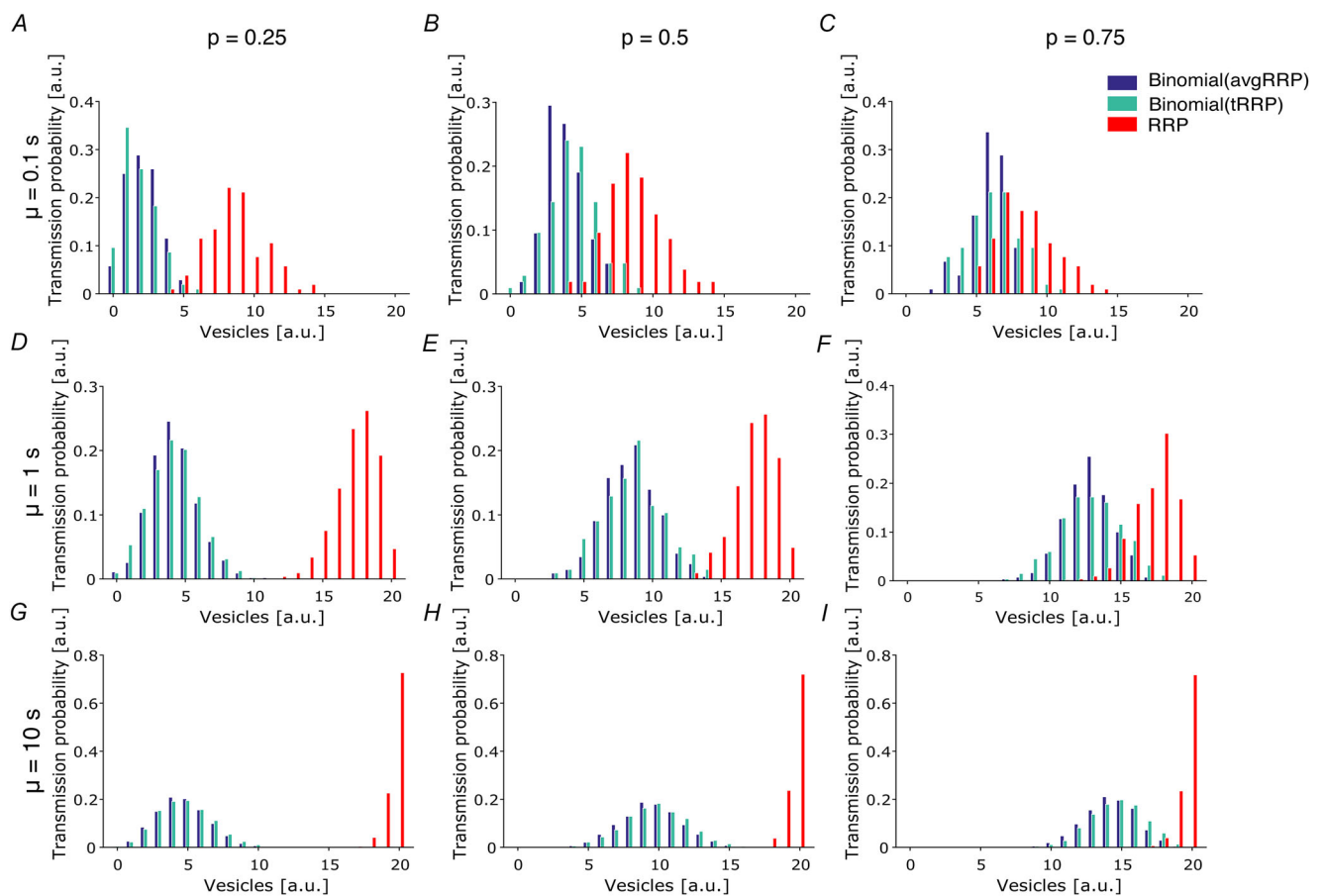

Figure 9. Analysis of simulated series of evoked vesicle fusion with dynamic RRP loaded by super-diffusive ($H = 0.9$) vesicle motion

A–I, histograms showing the frequencies of evoked transmission events (stimulation period 2 s) with varying number of vesicles present in the RRP, whose size is regulated by super-diffusive motion/docking of 20 vesicles (fBm with Hurst exponent $H = 0.9$) and their spontaneous fusion (see text for details). For each graph, blue bars show data from a binomial model with N equal to the average RRP, green bars show data from a binomial model with N equal to the instantaneous RRP (tRRP), and yellow bars show data from a $p = 1$ condition (fused vesicles = tRRP at stimulation time). *A–C*, simulations with mean spontaneous fusion time (T_{fuse}) $\mu = 0.1$ s and evoked fusion probability $p = 0.25$ (*A*), 0.5 (*B*), and 0.75 (*C*). *D–F*, simulations with mean spontaneous fusion time (T_{fuse}) $\mu = 1$ s and evoked fusion probability $p = 0.25$ (*D*), 0.5 (*E*), and 0.75 (*F*). *G–I*, simulations with mean spontaneous fusion time (T_{fuse}) $\mu = 10$ s and evoked fusion probability $p = 0.25$ (*G*), 0.5 (*H*), and 0.75 (*I*). [Colour figure can be viewed at wileyonlinelibrary.com]

In addition, by applying fractal analyses, namely the periodogram and the Allan factor, we obtained variable degrees of power-law behaviour (Fig. 2*E–H*), as previously found for real spontaneous release series (Lamanna et al., 2011, 2015; Lowen et al., 1997). Hence, based on our simulations and analyses, this model is able to reproduce both deviation from the Poisson hypothesis and power-law features for spontaneous quantal release series, thus suggesting that both these features could be related to diffusion processes going on inside the presynaptic compartment, as was previously suggested (Lamanna et al., 2015). Importantly, the Hurst exponent, which can be estimated through our model starting from experimental series, provides crucial information about the dynamics of vesicles motion inside the pre-

synaptic terminal. For instance, $H > 0.5$ (super-diffusion) suggests that vesicles motion is facilitated by molecular motors, while $H < 0.5$ (sub-diffusion) might indicate an over-crowded environment, possibly characterized by several vesicle clusters and low mobility, as well as by lack of active transport.

Finally, we performed simulations of evoked exocytosis based on a time-varying RRP, whose extension is regulated by the spontaneous release process described above, where a population of recycling vesicles intermittently dock, fuse and diffuse in the presynaptic compartment. Based on the analysis of synaptic transmission probability on these evoked transmission series we showed that, for certain values of the parameters, namely the Hurst exponent, the average time of spontaneous fusion,
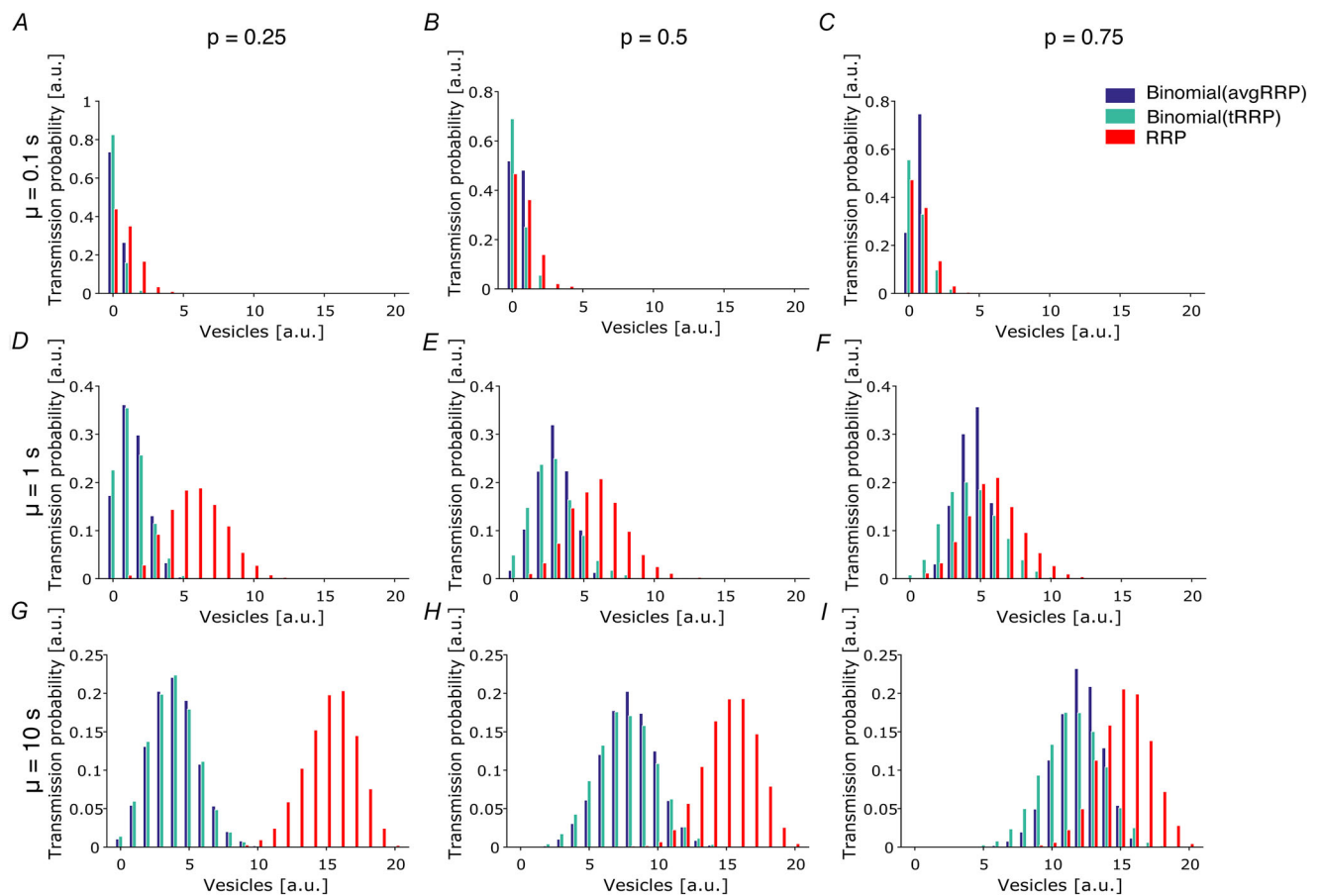

Figure 10. Analysis of simulated series of evoked vesicle fusion with dynamic RRP loaded by sub-diffusive ($H = 0.25$) vesicle motion

A–I, histograms showing the frequencies of evoked transmission events (stimulation period 2 s) with varying number of vesicles present in the RRP, whose size is regulated by sub-diffusive motion/docking of 20 vesicles (fBm with Hurst exponent $H = 0.25$) and their spontaneous fusion (see text for details). For each graph, blue bars show data from a binomial model with N equal to the average RRP, green bars show data from a binomial model with N equal to the instantaneous RRP (tRRP) and yellow bars show data from a $p = 1$ condition (fused vesicles = tRRP at stimulation time). *A–C*, simulations with mean spontaneous fusion time (T_{fuse}) $\mu = 0.1$ s and evoked fusion probability $p = 0.25$ (*A*), 0.5 (*B*), and 0.75 (*C*). *D–F*, simulations with mean spontaneous fusion time (T_{fuse}) $\mu = 1$ s and evoked fusion probability $p = 0.25$ (*D*), 0.5 (*E*), and 0.75 (*F*). *G–I*, simulations with mean spontaneous fusion time (T_{fuse}) $\mu = 10$ s and evoked fusion probability $p = 0.25$ (*G*), 0.5 (*H*), and 0.75 (*I*). [Colour figure can be viewed at wileyonlinelibrary.com]

such RRP dynamics might be sufficient to explain the large quantal variability in synaptic output without any binomial assumption (i.e. assuming evoked fusion probability $p = 1$). We also showed that, even assuming a binomial model with $p < 1$ and a time-varying RRP, the dynamics of the latter due to spontaneous activity and vesicle diffusion can significantly affect the synaptic output, and thus the estimation of p and N (where N is assumed to be stable). More importantly, such a result has deep implications in terms of emergence of power-law behaviour and fractal features in synaptic communication, and thus in neuronal activity in general, as these features could possibly be ultimately ascribed to vesicle diffusion, a microscopic-scale and very under-rated process when dealing with large neuronal networks.

In addition, such an alternative viewpoint suggests that the morphological properties of the presynaptic milieu, including its crowding level, but also other biophysical processes influencing vesicle motion, such as molecular motors (Peng et al., 2012) and vesicle clusters (Milovanovic & De Camilli, 2017; Reshetniak & Rizzoli, 2021), can have a direct impact on synaptic transmission probability (Holt et al., 2004; Park et al., 2022). In this context, several important physiological phenomena that lead to changes in presynaptic release probability, such as short-term and long-term potentiation, could be explained at least partially by relatively durable modifications of vesicle motion dynamics (Arikkath & Reichardt, 2008; Bourne et al., 2013; Chenouard et al., 2020; Schlüter et al., 2006; Staras et al., 2010).

Figure 11. Analysis of simulated series of evoked vesicle fusion with dynamic RRP loaded by super-diffusive (*H* = 0.75) vesicle motion

A–I, histograms showing the frequencies of evoked transmission events (stimulation period 2 s) with varying number of vesicles present in the RRP, whose size is regulated by super-diffusive motion/docking of 20 vesicles (fBm with Hurst exponent *H* = 0.75) and their spontaneous fusion (see text for details). For each graph, blue bars show data from a binomial model with *N* equal to the average RRP, green bars show data from a binomial model with *N* equal to the instantaneous RRP (tRRP) and yellow bars show data from a *p* = 1 condition (fused vesicles = tRRP at stimulation time). *A–C*, simulations with mean spontaneous fusion time (T_{fuse}) μ = 0.1 s and evoked fusion probability *p* = 0.25 (*A*), 0.5 (*B*), and 0.75 (*C*). *D–F*, simulations with mean spontaneous fusion time (T_{fuse}) μ = 1 s and evoked fusion probability *p* = 0.25 (*D*), 0.5 (*E*), and 0.75 (*F*). *G–I*, simulations with mean spontaneous fusion time (T_{fuse}) μ = 10 s and evoked fusion probability *p* = 0.25 (*G*), 0.5 (*H*), and 0.75 (*I*). [Colour figure can be viewed at wileyonlinelibrary.com]

Conclusions

In conclusion, we built a model of both spontaneous and evoked synaptic transmission, based on vesicle Brownian motions, that can reproduce several features of experimental synaptic release series, including deviation from the Poisson hypothesis and power-law behaviour. These results provide support for a possible physiological explanation of release process characteristics and dynamics which are still poorly understood. We believe that our model also supports the idea that the vesicular diffusive motions in a crowded environment, and the downstream RRP filling dynamics, are fundamental key factors regulating the efficacy of synaptic transmission.

Future routes of investigation will include extending the range of predictions of our model also to more complex processes such as short- and long-term synaptic plasticity, but also testing if different synaptic network topologies can change the non-linear features of neurotransmission (Schulte et al., 2018). The vast toolkit of methods now available to measure and manipulate synaptic transmission will make it feasible to achieve such aims in the near future (Lamanna, Ferro, et al., 2022). We hope that our computational results will foster the acquisition of novel experimental evidence to experimentally prove the relationship among these players, as well as their effects on neuronal communication.

Appendix

Derivation of the closed-closed form expression for the model's pdf with *H* = 0.5

The analytical solution to the convolution integral of eqn (7) was obtained using Wolfram Mathematica *Integrate* function and assuming $\lambda_1 > 0 \wedge \lambda_1 > 0 \wedge C > 0 \wedge x \geq 0$. Then, a simpler form was derived as follows:

$$f_{\text{rel}}(x) = \frac{\lambda_1\lambda_2}{2(\lambda_1 - \lambda_2)} \left(-e^{-iC\sqrt{2\lambda_1}-\lambda_1 x}\left(\text{erfc}\left(\frac{C}{\sqrt{2x}} - i\sqrt{\lambda_1 x}\right) + e^{2iC\sqrt{2\lambda_1}}\text{erfc}\left(\frac{C}{\sqrt{2x}} + i\sqrt{\lambda_1 x}\right)\right) \right.$$

$$\left. + e^{-iC\sqrt{2\lambda_2}-\lambda_2 x}\left(\text{erfc}\left(\frac{C}{\sqrt{2x}} - i\sqrt{\lambda_2 x}\right) + e^{2iC\sqrt{2\lambda_2}}\text{erfc}\left(\frac{C}{\sqrt{2x}} + i\sqrt{\lambda_2 x}\right)\right)\right)$$

$$= \frac{\lambda_1\lambda_2}{2(\lambda_1 - \lambda_2)} \left(-e^{-iC\sqrt{2\lambda_1}}e^{-\lambda_1 x}\text{erfc}\left(\frac{C}{\sqrt{2x}} - i\sqrt{\lambda_1 x}\right) - e^{iC\sqrt{2\lambda_1}}e^{-\lambda_1 x}\text{erfc}\left(\frac{C}{\sqrt{2x}} + i\sqrt{\lambda_1 x}\right) \right.$$

$$\left. + e^{-iC\sqrt{2\lambda_2}}e^{-\lambda_2 x}\text{erfc}\left(\frac{C}{\sqrt{2x}} - i\sqrt{\lambda_2 x}\right) + e^{iC\sqrt{2\lambda_2}}e^{-\lambda_2 x}\text{erfc}\left(\frac{C}{\sqrt{2x}} + i\sqrt{\lambda_2 x}\right)\right)$$

$$= \frac{\lambda_1\lambda_2}{2(\lambda_1 - \lambda_2)} \left(-e^{-\lambda_1 x}\left(e^{-iC\sqrt{2\lambda_1}}\text{erfc}\left(\frac{C}{\sqrt{2x}} - i\sqrt{\lambda_1 x}\right) + e^{iC\sqrt{2\lambda_1}}\text{erfc}\left(\frac{C}{\sqrt{2x}} + i\sqrt{\lambda_1 x}\right)\right) \right.$$

$$\left. + e^{-\lambda_2 x}\left(e^{-iC\sqrt{2\lambda_2}}\text{erfc}\left(\frac{C}{\sqrt{2x}} - i\sqrt{\lambda_2 x}\right) + e^{iC\sqrt{2\lambda_2}}\text{erfc}\left(\frac{C}{\sqrt{2x}} + i\sqrt{\lambda_2 x}\right)\right)\right). \tag{eqA1}$$

By applying the Schwarz reflection principle to the complementary error functions with negative imaginary arguments in eqn (A1), we get:

$$f_{\text{rel}}(x) = \frac{\lambda_1\lambda_2}{2(\lambda_1 - \lambda_2)} \left(-e^{-\lambda_1 x}\left(\overline{e^{iC\sqrt{2\lambda_1}}\text{erfc}\left(\frac{C}{\sqrt{2x}} + i\sqrt{\lambda_1 x}\right)} + e^{iC\sqrt{2\lambda_1}}\text{erfc}\left(\frac{C}{\sqrt{2x}} + i\sqrt{\lambda_1 x}\right)\right) \right.$$

$$\left. + e^{-\lambda_2 x}\left(\overline{e^{iC\sqrt{2\lambda_2}}\text{erfc}\left(\frac{C}{\sqrt{2x}} + i\sqrt{\lambda_2 x}\right)} + e^{iC\sqrt{2\lambda_2}}\text{erfc}\left(\frac{C}{\sqrt{2x}} + i\sqrt{\lambda_2 x}\right)\right)\right), \tag{eqA2}$$

which simplifies to the final expression reported in eqn (8):

$$f_{\text{rel}}(x) = \frac{\lambda_1\lambda_2}{2(\lambda_1 - \lambda_2)} \left(-e^{-\lambda_1 x}2Re\left(e^{iC\sqrt{2\lambda_1}}\text{erfc}\left(\frac{C}{\sqrt{2x}} + i\sqrt{\lambda_1 x}\right)\right) + e^{-\lambda_2 x}2Re\left(e^{iC\sqrt{2\lambda_2}}\text{erfc}\left(\frac{C}{\sqrt{2x}} + i\sqrt{\lambda_2 x}\right)\right)\right). \tag{eqA3}$$

References

Abenavoli, A., Forti, L., Bossi, M., Bergamaschi, A., Villa, A., & Malgaroli, A. (2002). Multimodal quantal release at individual hippocampal synapses: Evidence for no lateral inhibition. *Journal of Neuroscience*, **22**(15), 6336–6346.

Abenavoli, A., Forti, L., & Malgaroli, A. (2000). Mechanisms of spontaneous miniature activity at CA3-CA1 synapses: Evidence for a divergence from a random Poisson process. *The Biological Bulletin*, **199**(2), 184–186.

Arikkath, J., & Reichardt, L. F. (2008). Cadherins and Catenins at synapses: Roles in synaptogenesis and synaptic plasticity. *Trends in Neuroscience*, **31**(9), 487–494.

Böse, C. M., Qiu, D., Bergamaschi, A., Gravante, B., Bossi, M., Villa, A., Rupp, F., & Malgaroli, A. (2000). Agrin controls synaptic differentiation in hippocampal neurons. *Journal of Neuroscience*, **20**(24), 9086–9095.

Botev, Z. (2016). Fractional Brownian motion generator. *MATLAB Cent File Exch*. https://www.mathworks.com/matlabcentral/fileexchange/38935-fractional-brownian-motion-generator

Bourne, J. N., Chirillo, M. A., & Harris, K. M. (2013). Presynaptic ultrastructural plasticity along CA3→CA1 axons during long-term potentiation in mature hippocampus. *Journal of Comparative Neurology*, **521**(17), 3898–3912.

Bykowska, O., Gontier, C., Sax, A. L., Jia, D. W., Montero, M. L., Bird, A. D., Houghton, C., Pfister, J. P., & Costa, R. P. (2019). Model-based inference of synaptic transmission. *Frontiers in Synaptic Neuroscience*, **11**, 21.

Chanaday, N. L., & Kavalali, E. T. (2018). Optical detection of three modes of endocytosis at hippocampal synapses. *eLife*, **7**, e36097.

Chen, S., Yoo, H., Li, C. H., Park, C., Park, G., Tan, L. Y., Jung, S., & Park, H. (2021). Real-time three-dimensional tracking of single vesicles reveals abnormal motion and pools of synaptic vesicles in neurons of Huntington's disease mice. *Iscience*, **24**(10), 103181.

Chenouard, N., Xuan, F., & Tsien, R. W. (2020). Synaptic vesicle traffic is supported by transient actin filaments and regulated by PKA and NO. *Nature Communications*, **11**(1), 5318.

Chung, C. H., Barylko, B., Leitz, J., Liu, X., & Kavalali, E. T. (2010). Acute dynamin inhibition dissects synaptic vesicle recycling pathways that drive spontaneous and evoked neurotransmission. *Journal of Neuroscience*, **30**(4), 1363–1376.

Clauset, A., Shalizi, C. R., & Newman, M. E. J. (2007). Power-law distributions in empirical data. *Society of Indian Automobile Manufacturers Review*, **51**, 661–703.

Ding, M., & Yang, W. (1995). Distribution of the first return time in fractional Brownian motion and its application to the study of on-off intermittency. *Physical Review E*, **52**(1), 207–213.

Fatt, P., & Katz, B. (1952). Spontaneous subthreshold activity at motor nerve endings. *The Journal of Physiology*, **117**(1), 109–128.

Ferro, M., Lamanna, J., Ripamonti, M., Racchetti, G., Arena, A., Spadini, S., Montesano, G., Cortese, R., Zimarino, V., & Malgaroli, A. (2017). Functional mapping of brain synapses by the enriching activity-marker SynaptoZip. *Nature Communications*, **8**(1), 1229.

Forti, L., Bossi, M., Bergamaschi, A., Villa, A., & Malgaroli, A. (1997). Loose-patch recordings of single quanta at individual hippocampal synapses. *Nature*, **388**(6645), 874–878.

Granseth, B., Odermatt, B., Royle, S. J., & Lagnado, L. (2006). Clathrin-mediated endocytosis is the dominant mechanism of vesicle retrieval at hippocampal synapses. *Neuron*, **51**(6), 773–786.

Han, D., Korabel, N., Chen, R., Johnston, M., Gavrilova, A., Allan, V. J., Fedotov, S., & Waigh, T. A. (2020). Deciphering anomalous heterogeneous intracellular transport with neural networks. *eLife*, **9**, e52224.

Holt, M., Cooke, A., Neef, A., & Lagnado, L. (2004). High mobility of vesicles supports continuous exocytosis at a ribbon synapse. *Current Biology*, **14**(3), 173–183.

Joensuu, M., Padmanabhan, P., Durisic, N., Bademosi, A. T. D., Cooper-Williams, E., Morrow, I. C., Harper, C. B., Jung, W. R., Parton, R. G., Goodhill, G. J., Papadopulos, A., & Meunier, F. A. (2016). Subdiffractional tracking of internalized molecules reveals heterogeneous motion states of synaptic vesicles. *Journal of Cell Biology*, **215**(2), 277–292.

Kamin, D., Lauterbach, M. A., Westphal, V., Keller, J., Schönle, A., Hell, S. W., & Rizzoli, S. O. (2010). High- And low-mobility stages in the synaptic vesicle cycle. *Biophysical Journal*, **99**(2), 675–684.

Kavalali, E. T. (2015). The mechanisms and functions of spontaneous neurotransmitter release. *Nature Reviews Neuroscience*, **16**(1), 5–16.

Kneussel, M., & Wagner, W. (2013). Myosin motors at neuronal synapses: Drivers of membrane transport and actin dynamics. *Nature Reviews Neuroscience*, **14**(4), 233–247.

Kroese, D. P., & Botev, Z. I. (2013). Spatial Process Generation. 1–40.

Lamanna, J., Esposti, F., Malgaroli, A., & Signorini, M. G. (2011). Fractal behavior of spontaneous neurotransmitter release: From single-synapse to whole-cell recordings. In Proceedings of the Annual International Conference of the IEEE Engineering in Medicine and Biology Society, EMBS.

Lamanna, J., Ferro, M., Spadini, S., & Malgaroli, A. (2022). Exploiting the molecular diversity of the synapse to investigate neuronal communication: A guide through the current toolkit. *European Journal of Neuroscience*, **56**, 6141–6161.

Lamanna, J., Isotti, F., Ferro, M., Spadini, S., Racchetti, G., Musazzi, L., & Malgaroli, A. (2022). Occlusion of dopamine-dependent synaptic plasticity in the prefrontal cortex mediates the expression of depressive-like behavior and is modulated by ketamine. *Scientific Reports*, **12**(1), 11055.

Lamanna, J., Malgaroli, A., Cerutti, S., & Signorini, M. G. (2012). Detection of fractal behavior in temporal series of synaptic quantal release events: A feasibility study. *Computational Intelligence and Neuroscience*, **2012**, 704673.

Lamanna, J., Signorini, M. G., Cerutti, S., & Malgaroli, A. (2015). A pre-docking source for the power-law behavior of spontaneous quantal release: Application to the analysis of LTP. *Frontiers in Cellular Neuroscience*, **9**, 44.

Lowen, S. B., Cash, S. S., Poo, M., & Teich, M. C. (1997). Quantal neurotransmitter secretion rate exhibits fractal behavior. *Journal of Neuroscience*, **17**(15), 5666–5677.

Lowen, S. B., & Teich, M. C. (2005). *Fractal-based point processes*. John Wiley and Sons. http://books.google.com/books?id=iaH-3qqPq2IC&pgis=1

Malgaroli, A., Ting, A. E., Wendland, B., Bergamaschi, A., Villa, A., Tsien, R. W., & Scheller, R. H. (1995). Presynaptic component of long-term potentiation visualized at individual hippocampal synapses. *Science (80-)*, **268**(5217), 1624–1628.

Maschi, D., Gramlich, M. W., & Klyachko, V. A. (2018). Myosin V functions as a vesicle tether at the plasma membrane to control neurotransmitter release in central synapses. *eLife*, **7**, e39440.

McManus, O. B., Blatz, A. L., & Magleby, K. L. (1987). Sampling, log binning, fitting, and plotting durations of open and shut intervals from single channels and the effects of noise. *Pflügers Archiv – European Journal of Physiology*, **410**(4–5), 530–553.

Milovanovic, D., & De Camilli, P. (2017). Synaptic vesicle clusters at synapses: A distinct liquid phase? *Neuron*, **93**(5), 995–1002.

Neher, E., & Brose, N. (2018). Dynamically primed synaptic vesicle states: Key to understand synaptic short-term plasticity. *Neuron*, **100**(6), 1283–1291.

Park, C., Jung, S., & Park, H. (2022). Single vesicle tracking for studying synaptic vesicle dynamics in small central synapses. *Current Opinion in Neurobiology*, **76**, 102596.

Peng, A., Rotman, Z., Deng, P. Y., & Klyachko, V. A. (2012). Differential motion dynamics of synaptic vesicles undergoing spontaneous and activity-evoked endocytosis. *Neuron*, **73**(6), 1108–1115.

Rangarajan, G., & Ding, M. (2000). First passage time distribution for anomalous diffusion. *Physics Letters A*, **273**(5–6), 322–330.

Reshetniak, S., & Rizzoli, S. O. (2021). The vesicle cluster as a major organizer of synaptic composition in the short-term and long-term. *Current Opinion in Cell Biology*, **71**, 63–68.

Sara, Y., Virmani, T., Deák, F., Liu, X., & Kavalali, E. T. (2005). An isolated pool of vesicles recycles at rest and drives spontaneous neurotransmission. *Neuron*, **45**(4), 563–573.

Schikorski, T., & Stevens, C. F. (2001). Morphological correlates of functionally defined synaptic vesicle populations. *Nature Neuroscience*, **4**(4), 391–395.

Schlüter, O. M., Basu, J., Südhof, T. C., & Rosenmund, C. (2006). Rab3 superprimes synaptic vesicles for release: Implications for short-term synaptic plasticity. *Journal of Neuroscience*, **26**(4), 1239–1246.

Schulte, C., Lamanna, J., Moro, A. S., Piazzoni, C., Borghi, F., Chighizola, M., Ortoleva, S., Racchetti, G., Lenardi, C., Podestà, A., Malgaroli, A., & Milani, P. (2018). Neuronal cells confinement by micropatterned cluster-assembled dots with mechanotransductive nanotopography. *ACS Biomaterials Science & Engineering*, **4**(12), 4062–4075.

Sigworth, F. J., & Sine, S. M. (1987). Data transformations for improved display and fitting of single-channel dwell time histograms. *Biophysical Journal*, **52**(6), 1047–1054.

Silva, M., Tran, V., & Marty, A. (2021). Calcium-dependent docking of synaptic vesicles. *Trends in Neuroscience*, **44**(7), 579–592.

Sornette, D. (2006). *Critical phenomena in natural sciences: chaos, fractals, selforganization, and disorder: Concepts and tools*. 528. Springer Berlin, Heidelberg.

Staras, K., Branco, T., Burden, J. J., Pozo, K., Darcy, K., Marra, V., Ratnayaka, A., & Goda, Y. (2010). A vesicle superpool spans multiple presynaptic terminals in hippocampal neurons. *Neuron*, **66**(1), 37–44.

Thurner, S., Lowen, S., & Feurstein, M. (1997). Analysis, synthesis, and estimation of fractal-rate stochastic point processes. *Fractals*, **05**(04), 565–595.

Westphal, V., Rizzoli, S. O., Lauterbach , M. A., Kamin, D., Jahn, R., & Hell, S. W. (2008). Video-rate far-field optical nanoscopy dissects synaptic vesicle movement. *Science*, **320**(5873), 246–249.

Wilhelm, B. G., Groemer, T. W., & Rizzoli, S. O. (2010). The same synaptic vesicles drive active and spontaneous release. *Nature Neuroscience*, **13**(12), 1454–1456.

Zenlsek, D., Steyer, J. A., & Almers, W. (2000). Transport, capture and exocytosis of single synaptic vesicles at active zones. *Nature*, **406**(6798), 849–854.

Additional information

Data availability statement

The data supporting the findings are presented in the paper and are available upon reasonable request from the corresponding author. Code developed in MATLAB for model implementation and fitting is available at https://github.com/jacolamanna/quantal_release.

Competing interests

The authors declare no competing interests.

Author contributions

J.L. and A.M. designed the study. J.L. derived the analytical expressions. J.L. and A.M. performed and analysed the experiments. G.G. and J.L. performed data simulation and analyses. J.L. and A.M. provided supervision. A.V. collected electron microscopy images. G.G. and J.L. wrote manuscript draft. J.L. and A.M. wrote the final version of the manuscript. All authors have read and approved the final version of this manuscript and agree to be accountable for all aspects of the work in ensuring that questions related to the accuracy or integrity of any part of the work are appropriately investigated and resolved. All persons designated as authors qualify for authorship, and all those who qualify for authorship are listed.

Funding

None.

Supporting information

Additional supporting information can be found online in the Supporting Information section at the end of the HTML view of the article. Supporting information files available:

Peer Review History